Energy & Environmental Science

Identifying high performance and durable methylammonium-free lead halide perovskites through high throughput synthesis and characterization

Journal:	*Energy & Environmental Science*
Manuscript ID	EE-ART-08-2021-002691.R1
Article Type:	Paper
Date Submitted by the Author:	27-Oct-2021
Complete List of Authors:	An, Yu; Tianjin University, Castro, Andres; Georgia Institute of Technology, Materials Science and Engineering Li, Ruipeng; Cornell University, CHESS Hidalgo, Juanita; Georgia Institute of Technology, Materials Science and Engineering Perini, Carlo; Georgia Institute of Technology, Materials Science and Engineering Wang, Shirong; Tianjin University, Vagott, Jacob; Georgia Institute of Technology, Materials Science and Engineering Li, Xianggao; Tianjin University, Saidi, Wissam; University of Pittsburgh, Chemical Engineering Correa-Baena, Juan-Pablo; Georgia Institute of Technology, Materials Science and Engineering

Identifying high performance and durable methylammonium-free lead halide perovskites through high throughput synthesis and characterization

Yu An [a, b, c], Carlo Andrea Riccardo Perini [b], Juanita Hidalgo [b], Andrés-Felipe Castro-Méndez [b], Jacob N. Vagott [b], Ruipeng Li [d], Wissam A. Saidi [e], Shirong Wang [a,c], Xianggao Li [a,c] and Juan-Pablo Correa-Baena [b]**

[a] *School of Chemical Engineering and Technology, Tianjin University, Tianjin, 300072, China*

[b] *School of Materials Science and Engineering, Georgia Institute of Technology, Atlanta, Georgia, 30332, United States*

[c] *Collaborative Innovation Center of Chemical Science and Engineering (Tianjin), Tianjin, 300072, China*

[d] *National Synchrotron Light Source II, Brookhaven National Lab, Upton, New York, 11973, United States*

[e] *Department of Mechanical Engineering and Materials Science, University of Pittsburgh, Pittsburgh, PA 15261, USA*

**Corresponding Authors: X. Li lixianggao@tju.edu.cn; JPCB jpcorrea@gatech.edu*

Broader Context (no more than 200 words)

Metal halide perovskite solar cells are presently attracting immense interest due to the rapid rise of their solar to electric power conversion efficiency from 3.8% to over 25.5% within the past decade. The latest improvements have been achieved by compositional engineering. Methylammonium iodide (MAI)-free perovskites are promising for their high stability compared to those containing MAI, however, there is very little understanding on the role of phases and structures on all properties of the materials and devices. Here we present a systematic study of the compositional space of tunable formamidinium/cesium and iodide/bromide perovskites. Employing advanced X-ray scattering techniques with grazing incidence we elucidate the type of structures forming on the perovskites with 49 different compositions. Our findings give new sights for MAI-free materials towards understanding the mechanisms that make these perovskites efficient light harvesters and optimized compositions in perovskite solar cells towards long-term durability.

Abstract

One of the organic components in the perovskite photo-absorber, the methylammonium cation, has been suggested to be a roadblock to long-term operation of organic-inorganic hybrid perovskite-based solar cells. In this work we systematically explore the crystallographic and optical properties of the compositional space of mixed cation and mixed halide lead perovskites, where formamidinium (FA^+) is gradually replaced by cesium (Cs^+), and iodide (I^-) is substituted by bromide (Br^-), i.e., $Cs_yFA_{1-y}Pb(Br_xI_{1-x})_3$. Higher tolerance factors lead to more cubic structures, whereas lower tolerance factors lead to more orthorhombic. We find that while some correlation exists between tolerance factor and structure, tolerance factor does not provide a holistic understanding of whether a perovskite structure will fully form. By screening 26 solar cells with different compositions, our results show that $Cs_{1/6}FA_{5/6}PbI_3$ delivers the highest efficiency and long-term stability among I-rich compositions. This work sheds light on the fundamental structure-property relationships in the $Cs_yFA_{1-y}Pb(Br_xI_{1-x})_3$ compositional space, providing vital insight to the design of durable perovskite materials. Our approach provides a library of structural and optoelectronic information of this compositional space.

Keywords: perovskite, methylammonium-free, compositional engineering

Introduction

Since they were first reported in 2009 with a power conversion efficiency (PCE) of 3.8% [1], organic-inorganic hybrid perovskites have witnessed an unprecedented efficiency progress over a decade, resulting in the most recent highest certified PCE of 25.5% [2], which is approaching the 33.7% Shockley-Queisser (SQ) limit of single-junction solar cells [3]. The large number of constituents that can be fit into the ABX_3 crystal formula provides a relatively broad material space to be explored, where A is a monovalent cation (methylammonium — MA^+, formamidinium — FA^+, or cesium — Cs^+) [4,5], B is a divalent metal cation (typically Pb^{2+} or Sn^{2+}) [6], and X is a halogen anion (Cl^-, Br^- or I^-) [7]. Due to the tunability of its composition and bandgap, lead halide perovskites carry promise as the top wide-gap absorbers in silicon tandem solar cells or to be assembled into pure perovskite tandem cells, enabling higher efficiencies and bypassing the theoretical efficiency limit on single-junction solar cells. In addition, these lead halide perovskite materials allow for a range of versatile processing methods and a variety of cell structures [5], making halide perovskites a major competitor for low-cost solar energy conversion whether as stand-alone cells or as top cells in tandem structure [7–10]. Thus, understanding the relation between compositional variations and changes in crystal structure and bandgap becomes paramount for the design of optimum materials for different applications.

Despite the success of perovskite solar cells (PSCs) in laboratory research, the most pressing issue to be solved before commercialization is long-term stability, which is limited by a variety of factors, including chemical decomposition, phase transitions, or phase segregation. The extensively studied $MAPbI_3$ undergoes a phase transition above 57℃, and decomposes into PbI_2 even in an inert atmosphere at 85℃ owing to degassing MA^+ [11]. Mixed I/Br perovskites $MAPb(Br_xI_{1-x})_3$ that enable wider bandgaps are prone to phase segregation into iodide-rich and bromide-rich domains under illumination [12,13]. In addition, mixed-halide perovskite compositions are prone to the formation of halide vacancies, which introduce sub-bandgap energy levels [14] that act as trap states fostering non-radiative recombination, limiting the open-circuit voltage (V_{oc}) of the PSCs, and affecting the device photostability [13,15,16].

$FAPbI_3$ and $CsPbI_3$ have higher thermal-decomposition temperatures with respect to $MAPbI_3$, and have emerged as compelling candidates for the commercialization of long-term operating devices [17,18]. $FAPbI_3$ has an optical bandgap of 1.48 eV [19], closer to the theoretically optimal bandgap 1.34 eV [3] for a single-junction solar cell than the 1.58 eV of $MAPbI_3$ [19,20]. $CsPbI_3$

is promising for application in tandems and for its inorganic nature, which allows it to tolerate high temperatures without decomposition. Cs^+ has a considerably smaller radius (1.67 Å) than MA^+ (2.17 Å) and FA^+ (2.53 Å) [21,22], which results in a bandgap widened to 1.73eV for $CsPbI_3$ [19,23]. However, the black perovskite phases α-$FAPbI_3$ or α-$CsPbI_3$, which are suitable for efficient photon absorption and electron transport, are prone to structural instability, spontaneously converting into the undesirable non-photoactive yellow δ-phase in the ambient atmosphere [24–26]. Therefore, the main challenge on $FAPbI_3$ and $CsPbI_3$-based solar cells is to stabilize the black α-phase at room temperature.

To boost thermal and structural stabilities, as well as to inhibit halide segregation, it has been shown that mixing A-site cations in compositional engineering is essential [4,24,27]. Introducing small amounts of MA^+ in FA^+-based compositions enables suppressing the formation of the yellow δ-$FAPbI_3$ component due to stronger interaction via H…I–H (hydrogen bonding) or Coulomb interaction between the more polar MA^+ and the PbI_6 octahedral cage [28], while enabling high PCEs [7,24,29]. For mixed-cations with Cs^+ and MA^+, Niu et al. found a small addition of Cs^+ was responsible for inducing oriented polycrystalline films, leading to reduced series resistance and suppressing the formation of trap states, thus enhancing the PCE [30]. Introducing the small inorganic cation Cs^+ in FA-based compositions has been shown to adjust the strain in the structure to stabilize the α-$FAPbI_3$ [26]. The mixed-cation Cs^+/FA^+ perovskite showed an α phase even at room temperature, which is in contrast to pure $FAPbI_3$ (165℃) and $CsPbI_3$ (315℃), as well as excellent phase stability at high temperature or humidity conditions [8,26,31,32]. The obtained perovskite α-phase with FA^+ and Cs^+ is entropically stabilized, stemming from the α-phase of $CsPbI_3$ and $FAPbI_3$, which have similar structural features (corner-sharing PbI_6 octahedra) and volume [33]. Furthermore, mixed-cation Cs^+/FA^+ has been shown to lower the ionic mobility and suppress halide segregation, in contrast to $MAPb(Br_xI_{1-x})_3$ [13] and $FAPbI_yBr_{3-y}$ [19,34], by enhanced crystallinity to restrain the regions of short-range crystalline order, thus improving the compositional photostability and V_{oc} [7–9,27]. Therefore, mixed-cation Cs^+/FA^+, i.e., MA-free composition, is highly desired for the long-term operation.

Almost all high efficiency and phase-stable PSCs are fabricated by simultaneously integrating mixed A-site cations with mixed X-site halogens [4,5,24,35,36]. However, the fundamental understanding of the relation between composition variations and the structural and optoelectronic properties have not been fully revealed in the $Cs_yFA_{1-y}Pb(Br_xI_{1-x})_3$ compositional space. This work

systematically explores the compositional space of the $Cs_yFA_{1-y}Pb(Br_xI_{1-x})_3$ perovskites by simultaneously and independently changing the Cs^+/FA^+ and Br^-/I^- ratios. Our investigation highlights the structure-property relationships in the $Cs_yFA_{1-y}Pb(Br_xI_{1-x})_3$ compositional space by exploring optical and crystallographic properties through high throughput synthesis and characterization. An empirical equation for $Cs_yFA_{1-y}Pb(Br_xI_{1-x})_3$ bandgap as a function of composition is quantitatively determined, which contributes to tailor bandgaps suitable for single-junction and tandem applications. The crystal structure and phases in the $Cs_yFA_{1-y}Pb(Br_xI_{1-x})_3$ compositional space are identified qualitatively based on the results from synchrotron-based grazing incidence wide-angle X-ray scattering (GIWAXS). We find that tetragonal, cubic, and unidentified structures can be synthesized with slight compositional changes of I-rich $Cs_yFA_{1-y}Pb(Br_xI_{1-x})_3$ perovskites, and resulting in small effects to their electronic response in solar cells. A tetragonal structure is majority FA and I-based yielded the highest performance, regardless of annealing temperature (65℃ and 150℃). The work illustrates the importance of the precise composition of the perovskite for making devices with high performance and durability, and will help to extend the compositional design of novel MA-free perovskite for various optoelectronic applications.

Results and Discussion

A graphical illustration of the $Cs_yFA_{1-y}Pb(Br_xI_{1-x})_3$ composition space explored in this work is shown in Fig. 1A. A full set of 49 perovskite compositions with varying ratios of Cs^+/FA^+ and Br^-/I^- was deposited via solution processing. The 49 films were prepared by combining perovskite stock solutions in the appropriate molar ratio to obtain the desired $Cs_yFA_{1-y}Pb(Br_xI_{1-x})_3$ final composition. Four 0.4 M master solutions were prepared (i.e., $CsPbI_3$, $FAPbI_3$, $CsPbBr_3$, and $FAPbBr_3$) in dimethyl sulfoxide (DMSO). The perovskite solution stoichiometries are correlated with the respective sample numbers in Fig. 1A. A mild annealing temperature of 65℃ was selected to retain the perovskite phase of the Cs-rich films (Fig. S1) [9]. The annealing at 65°C is too low to crystallize the perovskite phase in FA-only films (especially No.43-No.46), which, however, have been studied extensively in previous reports [19,29]. The 49 perovskite films present markedly different colors across the matrix of variations, as illustrated in a photograph in Fig.1B. I-rich films are generally dark brown and Br-rich films are progressively more orange, then turning to yellow, with increasing bromide content. The $FAPbI_3$ film does not show the dark brown color expected for the α phase, as the annealing temperature selected is lower than the phase transition temperature

of 160℃ [25]. All films (except the pure Cs-based compositions, No.1-No.7) annealed at 170 ℃ were also prepared and are presented in Fig. S1, and it is important to note that these samples degraded within minutes, and thus we excluded these samples from further characterization. Herein, all characterizations on films are performed on perovskites annealed at 65 ℃, except when otherwise specified to ensure all conditions are kept constant in the study.

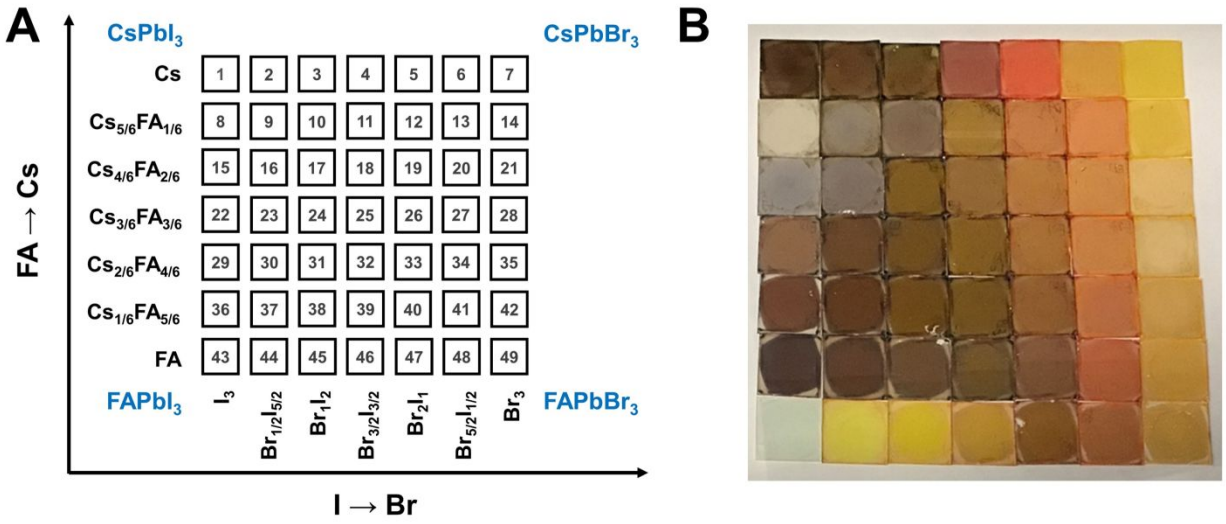

Fig.1. (A) Schematic illustration of the compositional matrix with notations for all the compositions explored. The numbers on the squares represent the key between the perovskite compositions and the corresponding sample numbers. (B) Photograph of the full set of perovskite films arranged in the same order as in the composition matrix of (A).

Crystallographic properties

Tuning the Goldschmidt tolerance factor (t) through compositional engineering is a practical approach to tailor the crystallographic properties and structural stability of perovskite materials [21,26,29]. The t is a reliable empirical index used to predict the structural phase of a perovskite by evaluating its ionic size mismatch. The expression is $t = \frac{r_A + r_X}{\sqrt{2}(r_B + r_X)}$, where r_A, r_B and r_X are the radii of the A cation, B cation, and X anion, respectively. Here, it is widely understood that t equals 1 for a perfect cubic perovskite. Values of t in the range 0.9-1.0 mostly result in cubic perovskites at room temperature. The t values between 0.8-0.9 favor distorted corner-sharing octahedra configurations, which result in perovskite structures of lower symmetry than cubic, e.g., orthorhombic or tetragonal [21,26,29]. The t values greater than 1.0, induce a hexagonal non-perovskite structure with face-sharing octahedra. While this is the general understanding in the field, in this study we attempt to explore, experimentally, the relationship

between *t* and different structures. For a composition such as $Cs_yFA_{1-y}Pb(Br_xI_{1-x})_3$, the weighted average at the A- and X-site of the two different ions is used to define an effective ionic radius [26] to compute the tolerance factor.

$$r_{X\text{ - effective}} = x r_{Br^-} + (1-x) r_{I^-}$$

$$r_{A\text{ - effective}} = y r_{Cs^+} + (1-y) r_{FA^+}$$

$$t_{effective} = \frac{r_{A\text{ - effective}} + r_{X\text{ - effective}}}{\sqrt{2}\,(r_{Pb^{2+}} + r_{X\text{ - effective}})} \quad (1)$$

The computed $t_{effective}$ for the different compositions are summarized in Fig.2 assuming r_{Cs^+} = 1.67 Å, r_{FA^+} = 2.53 Å, $r_{Pb^{2+}}$ = 1.19 Å, r_{Br^-} = 1.96 Å, r_{I^-} = 2.20 Å [21,22,37]. The $t_{effective}$ in Fig.2 could thus be used to roughly predict the structure of the different perovskite compositions. The $t_{effective}$ values of 47 of the 49 compositions fall into the range 0.8-1.0 suggesting that these perovskite structures will form corner-sharing octahedra. $FAPbBr_3$ and $FAPbBr_{1/2}I_{5/2}$ have $t_{effective}$ slightly larger than one, however, estimating the ionic radius of the organic FA^+ is complex and prone to errors [38], making these two compositions still promising candidates to process perovskites with cubic structure. Of the other 47 compositions, FA-rich compositions, i.e., No. 24-47, should be prone to form a cubic structure, whereas Cs-rich compositions, i.e., No. 1-23, are likely to form perovskite structures with low crystal symmetry.

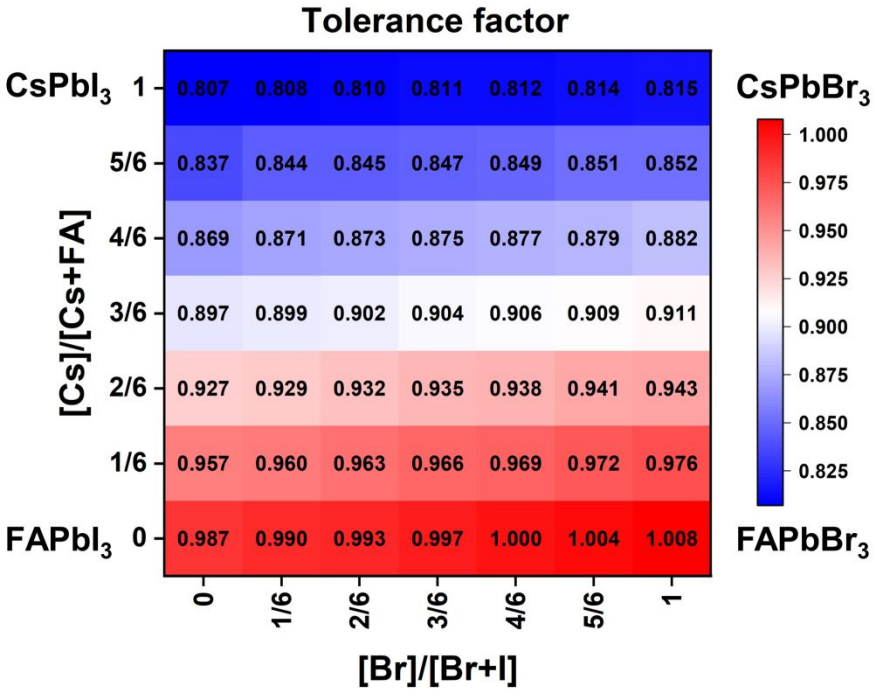

Fig.2. Effective tolerance factor map for the $Cs_xFA_{1-x}Pb(Br_yI_{1-y})_3$ compositional space tuned by composition engineering.

To reveal the correlation between composition and crystal phase, X-ray diffraction (XRD) and GIWAXS were performed. Perovskite crystals exhibit polymorphism, different crystal phases can thus be formed depending on the free energy of formation, preparation conditions, and temperature. For instance, $CsPbI_3$ has three black photoactive perovskite phases - namely, the α- (cubic), β- (tetragonal), and γ-phases (orthorhombic), and one yellow photoinactive non-perovskite δ-phase (orthorhombic) made of edge-sharing PbI_6 octahedra, as illustrated in Fig. 3A-D. Similar to $CsPbI_3$, $FAPbI_3$ exhibits two main phases: a black cubic perovskite α-phase and a yellow hexagonal non-perovskite δ-phase with face-sharing 1D PbI_6 octahedra (Fig. 3E) [38]. The α-, β-, and γ-phases are all composed of corner-sharing PbI_6 octahedra, but have decreasing crystal symmetry as the distortion of the PbI_6 octahedra increases (Fig. 3A-C). The decrease in symmetry is reflected in peak splitting and the appearance of additional peaks in the XRD pattern (Fig. 3F). As an example, the $(100)_C$ reflection at around $q = 1.0$ Å^{-1} of the α-phase ($Pm\bar{3}m$) in Fig. 3F splits into the $(110)_T$, $(001)_T$ reflections and $(110)_O$, $(002)_O$ reflections in the β-phase ($P4\bar{m}bm$) and γ-phase ($Pbnm$), respectively [39]. Here, the subscript of the crystal plane represents the corresponding crystal phase, i.e., C, T, and O represent cubic, tetragonal and orthorhombic, respectively. It is notable that there is still the same number of splitting peaks when moving from tetragonal to orthorhombic. In addition, the difference in *d*-spacing among cubic, tetragonal and orthorhombic is usually sufficiently small that the splitting can be difficult to resolve. Hence, it is challenging to identify the crystal phase by means of split peaks, especially for tetragonal and orthorhombic structures. In the β-phase, the $(210)_T$ and $(211)_T$ reflections appear at around $q = 1.6$ Å^{-1}and 1.9 Å^{-1}, respectively, (shown in the red area of Fig. 3F), comparing to the α-phase with undistorted PbI_6 octahedra. In the γ-phase with a second distortion in the orthorhombic structure, the crystal symmetry is lower and a new reflections appears around $q = 1.7$ Å^{-1} (shown in the blue area of Fig. 3F), corresponding to the $(211)_O$, $(121)_O$, $(103)_O$ planes. Hence, the characteristic peaks at around $q = 1.6$ Å^{-1} and 1.9 Å^{-1} could be used to distinguish whether the tetragonal phase exists, while the peak around $q = 1.7$ Å^{-1} could be used to identify if an orthorhombic phase is present [40–43].

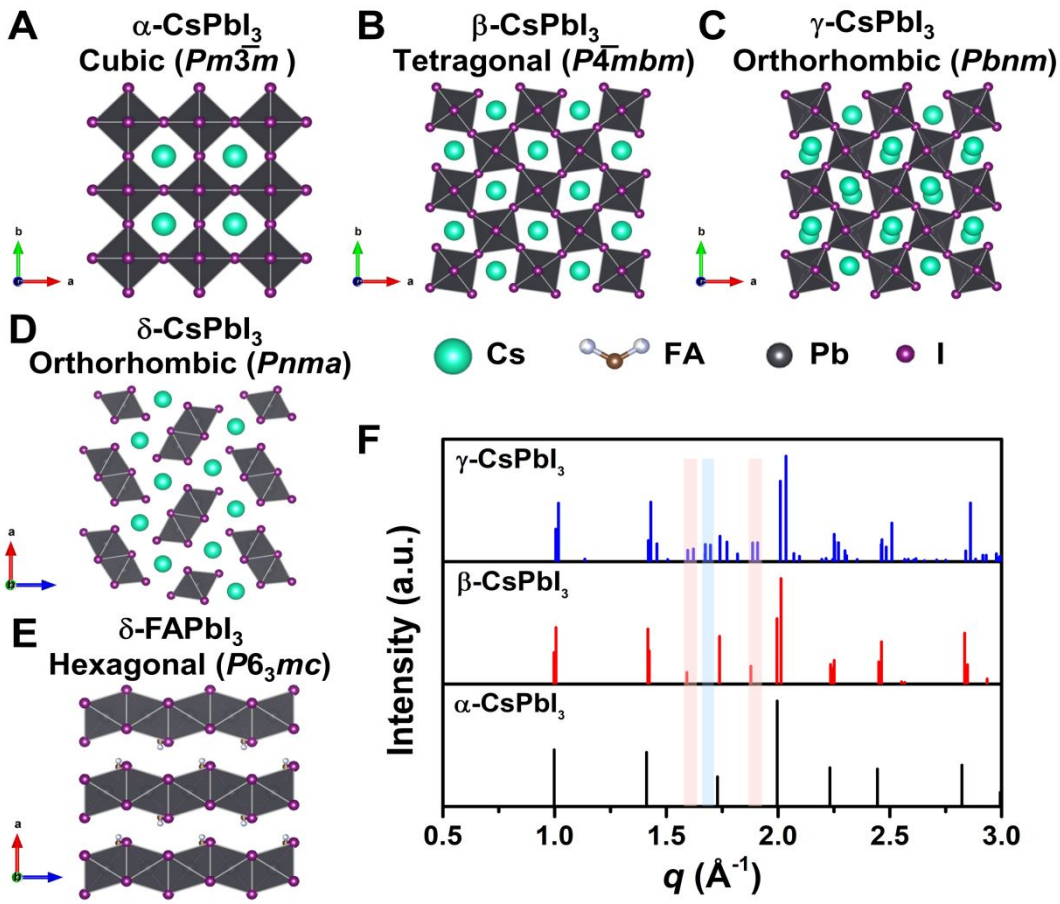

Fig.3. Crystal structure of three perovskite phases with corner-sharing octahedra for $CsPbI_3$, which are cubic α-$CsPbI_3$ (A), tetragonal β-$CsPbI_3$ (B), and orthorhombic γ-$CsPbI_3$ (C). (D) and (E) are crystal structure of non-perovskite δ-$CsPbI_3$ and δ-$FAPbI_3$, respectively. All the crystal structures in A-E were plotted by Vesta by using crystallographic information files extracting from references [25,44,45]. (F) Simulated powder XRD patterns for α-, β-, and γ- phases of $CsPbI_3$ plotted with vertical lines corresponding to the diffraction peaks. XRD patterns plotted with respect to scattering vector q, which is equivalent to $2*\pi/d$ where d is the d-spacing of the diffracting set of planes. The red area shows the positions of the extra XRD peaks discussed in the main text for tetragonal and orthorhombic structures compared with cubic structure. The blue area exhibits the position of the additional XRD peak discussed in the main text for orthorhombic structures compared with cubic and tetragonal structures. XRD pattern was simulated by Vesta.

Since I^- is larger than Br^-, there should be a lattice contraction when Br^- substitutes for I^-, thus giving rise to a smaller d-spacing. Based on Bragg's law, a corresponding shift in XRD peaks towards a larger diffraction angle is expected upon increasing bromine content. A shift towards a larger angle is likewise anticipated as smaller Cs^+ substitutes for FA^+. Such trends are indeed observed in the XRD diffraction patterns shown in Fig. 4. The XRD patterns for all compositions and peak-shifts for all subsets are available in Fig. S2-S3. The XRD peak at 14.0° shifts to a higher

angle with increasing Br^- content demonstrating the incorporation of Br^- in the perovskite lattice (Fig. 4A-B). The XRD peak at 14.8° shifts to higher angle with increasing Cs^+content reveals that as FA^+ is replaced with Cs^+ (Fig. 4C-D). The XRD peak at ~14-15° for the compositions in the matrix usually exhibits single peak, whereas some compositions show split peaks. For instance, $Cs_{2/6}FA_{4/6}PbBr_3$ (No.35) in Fig. 4D shows a split peak at around 15.0°, which may be associated with a decrease in crystal symmetry. In addition, $CsPbBr_{1/2}I_{5/2}$ (No.2) and $Cs_{4/6}FA_{2/6}Pb(Br_xI_{1-x})_3$ ($1/2 \leq x \leq 2$, i.e., No.16-19) also show apparent peak splitting (Fig. S2-S3), related to low crystal symmetry. The films with high bromide content or high cesium content exhibit high texture by having only a few dominant peaks (Fig. 4A and 4C).

The crystal symmetries of the four corner compounds (i.e., $CsPbI_3$, $CsPbBr_3$, $FAPbI_3$, and $FAPbBr_3$) were then analyzed to further elucidate which crystal phases form depending on the compositions studied. The as-deposited $CsPbI_3$ film in a nitrogen glovebox was dark brown (Fig. 1B), but converts to visible yellow in few minutes once exposed to ambient atmosphere. The XRD pattern of $CsPbI_3$ film in Fig. S4A indicates that $CsPbI_3$ has mixed γ-$CsPbI_3$ perovskite phase and orthorhombic δ-$CsPbI_3$ (*Pnma*) non-perovskite phase since it was measured at ambient condition, in agreement with the reported structures and the metastability of γ-$CsPbI_3$ [25,44,46]. The peaks located at 14.41°, 20.29°, and 28.90° are indexed as the (110), (112) and (220) planes in sequence for the orthorhombic *Pbnm* γ-$CsPbI_3$ phase [44]. The characteristic diffraction peaks at 9.86° and 13.06° correspond to the (101) and (102) planes of yellow orthorhombic *Pbnm* δ-$CsPbI_3$ [25]. For the $CsPbBr_3$ film, the two strong peaks at 15.25° and 30.74° in the XRD pattern (Fig. S4B) matched well with the (110) and (220) planes of the standard orthorhombic perovskite structure [9,47,48]. These two strong diffraction peaks dominate the XRD pattern of the $CsPbBr_3$ film, underlining the presence of a high degree of texture. The XRD of the $FAPbI_3$ film (Fig. S4C) is in good agreement with literature data for the hexagonal $P6_3mc$ δ-$FAPbI_3$ structure at room temperature and ambient conditions [25]. Likewise, $FAPbBr_3$ (Fig. S4D) exhibits a cubic $Pm\bar{3}m$ structure at room temperature that is in line with previous reports [19,29,49].

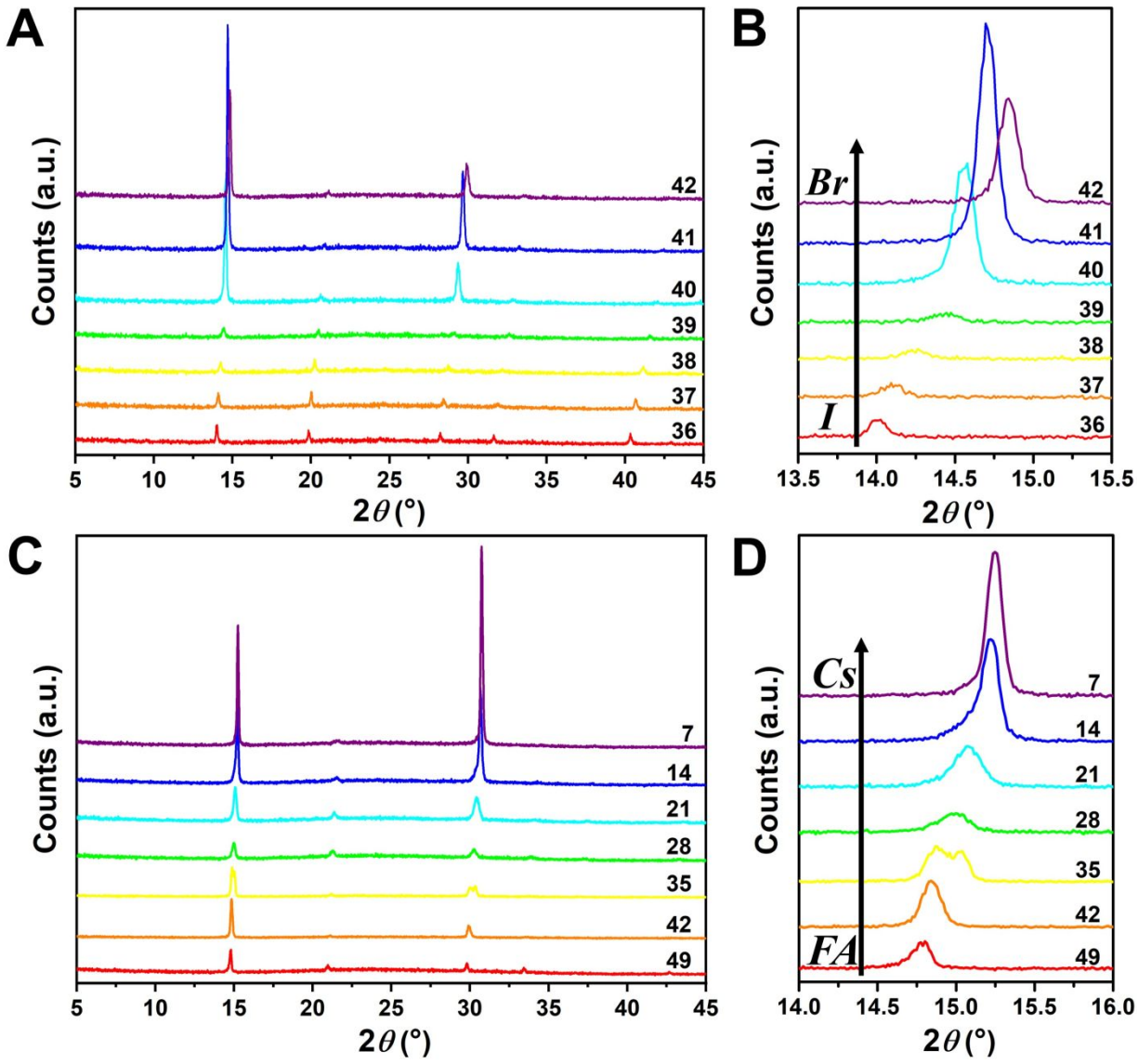

Fig.4. XRD patterns of $Cs_{1/6}FA_{5/6}Pb(Br_xI_{1-x})_3$ films as a function of Br content (A and B) and $Cs_yFA_{1-y}PbBr_3$ as a function of Cs content (C and D). B and D are zoom-ins of the peaks at ~14-15 degree in (A) and (B).

Although the presence of XRD peak splitting could give the information for the decreased crystal symmetry for some compositions, e.g., No.16-19 in $Cs_{4/6}FA_{2/6}PbBr_xI_{1-x}$, the films with high texture only show a few predominant signals, possibly hiding some characteristic peaks and making it hard to distinguish which crystal phases are present in the film. Due to its measurement geometry of grazing-incidence, GIWAXS technique provides signal that is independent from texture effects that can hide real peak signals, and thus it is perfectly suited for the investigation of the crystallographic information of thin films compared to conventional XRD. To better identify which crystal phases are present in the matrix, synchrotron-based GIWAXS was performed. The

GIWAXS results for identification of the crystal phase of the four corner compounds (Fig. S5-6) are consistent with the XRD data, except the $CsPbI_3$, which only exhibits δ-$CsPbI_3$ phase due to the phase transition that was induced during the measurements at ambient conditions. The four characteristic peaks with low signal at q = 1.7-2.0 $Å^{-1}$ of $CsPbBr_3$ shown in GIWAXS data (Fig. S5) show that the as-deposited $CsPbBr_3$ is orthorhombic phase [9,47,48] while those subtle signals are hidden in XRD (Fig. 4C) due to the high texture. Therefore, the GIWAXS data was used to qualitatively identify the phase variation in the matrix. As revealed in Fig. 5A, there are two extra peaks that appear for some compositions (i.e., No.36 and No. 40-42) in $Cs_{1/6}FA_{5/6}Pb(Br_xI_{1-x})_3$ at around q = 1.6 $Å^{-1}$ and 1.9 $Å^{-1}$ corresponding to the $(210)_T$ and $(211)_T$ reflections. The data then suggests that composition No.36 and No. 40-42 have a tetragonal symmetry, while composition No.37-39 in $Cs_{1/6}FA_{5/6}Pb(Br_xI_{1-x})_3$ with mixed halide and low bromide content are cubic since those two peaks are absent in their integrated GIWAXS patterns. Here, halide segregation could be excluded because pure-Br $Cs_{1/6}FA_{5/6}PbBr_3$ (No.42) also has the characteristic peaks for a tetragonal symmetry (Fig. 5a). It is also possible that No.36 and No. 40-42 are a mixture of tetragonal and cubic phases. However, it is challenging to rigorously quantify the amounts of each phase present with established techniques since our samples are thin films. Therefore, here we discuss the lowest crystal symmetry that is present in the GIWAXS data. Furthermore, octahedra tilting and the orthorhombic phase is present in Cs-rich compositions No.2, No.9, and No.16 of $Cs_yFA_{1-y}PbBr_{1/2}I_{5/2}$ as shown by an extra reflection at around q = 1.7 $Å^{-1}$(Fig. 5B), assigned to three reflections $(211)_O$, $(121)_O$, $(103)_O$. This decreased symmetry is also in accordance with the split peaks observed in XRD and is in line with calculated tolerance factors predicting low symmetry (Fig. 2). There are clear splitting peaks around 14.45° and 29.07° in the XRD pattern of composition No.2 (Fig. S3). Composition No.9 shows the shoulder peaks closely near the high-intensity peaks at 20.45° and 45.51° (Fig. S3). Composition No.16 grows clear splitting peaks around 14.34°, 20.22°, 28.89° and 41.32° (Fig. S3). The full set of GIWAXS patterns could be found in Fig. S5-6. In addition, the trends in GIWAXS are that the peaks will shift to higher q values, which indicate the decreased lattice d-spacing and lattice contraction upon increasing in the bromide content (Fig. 5A) or cesium content (Fig. 5B). This is in line with the observation in XRD data, again corroborating the incorporation of halide and A-site cation into the crystal lattice.

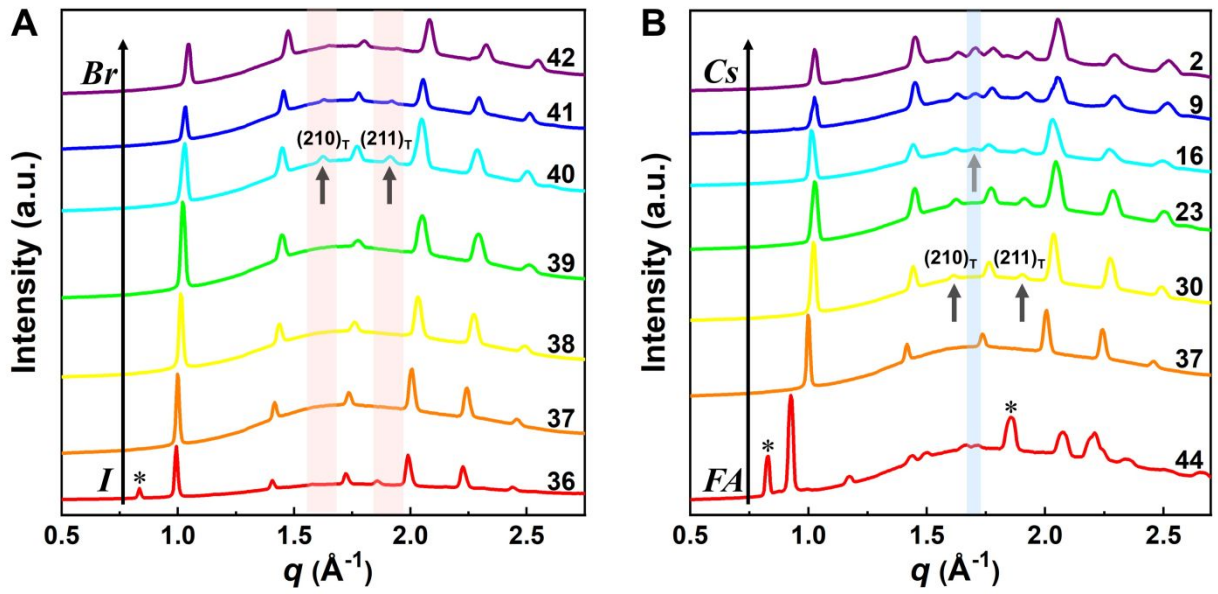

Fig.5. Integrated circular average of 2D GIWAXS patterns for $Cs_{1/6}FA_{5/6}Pb(Br_xI_{1-x})_3$ films as a function of Br content (A) and $Cs_yFA_{1-y}PbBr_{1/2}I_{5/2}$ as a function of Cs content (B). δ-$FAPbI_3$ was marked by *. The black arrows point to the characteristic peaks of tetragonal phase and the grey arrow refers to the characteristic peaks of orthorhombic phase, i.e., $(211)_O$, $(121)_O$, $(103)_O$.

The clear evidence for the variation of crystal symmetry motivates us to qualitatively establish the relationship between crystal symmetry and perovskite compositions. Combining the information retrieved from XRD and GIWAXS data, we identify the presence of perovskite and non-perovskite phases as a function of composition in Fig. 6A. We observe that iodine-pure compositions are prone to the formation of secondary non-perovskite phases. The $Cs_yFA_{1-y}PbI_3$, $FAPbI_3$ (No.43) and $Cs_{1/6}FA_{5/6}PbI_3$ (No.36) perovskite thin films have non-perovskite δ-$FAPbI_3$ phase, and the other five compositions with Cs ratio in the range of $2/6 \leqslant y \leqslant 1$ show signatures of the presence of the non-perovskite δ-$CsPbI_3$ phase (Fig. S6). The ratio of non-perovskite phase to perovskite phase for $Cs_yFA_{1-y}PbI_3$ compositions is estimated by calculating the intensity ratio of the characteristic peak at $q = 0.70$ Å^{-1} (δ-$CsPbI_3$) or $q = 0.83$ Å^{-1} (δ-$FAPbI_3$) for non-perovskite phase over the characteristic peak at q around 1.00 Å^{-1} of perovskite phase was calculated based on GIWAXS data in $Cs_yFA_{1-y}PbI_3$ compositions, as shown in Fig. S7. The content of δ-$FAPbI_3$ dramatically decreases when 1/6 of FA^+ is replaced by Cs^+, i.e., $Cs_{1/6}FA_{5/6}PbI_3$ (No.36). As the ratio of Cs increases, so does the content of δ-$CsPbI_3$ in the range of $2/6 \leq y \leq 1$. The presence of different non-perovskite phases as a function of composition and the boundary at around $1/6 < y < 2/6$ might be explained by changes in the formation energy between the corresponding perovskite

phases and two non-perovskite phases. It has been calculated that δ-$CsPbI_3$ has lower formation energy than that of δ-$FAPbI_3$ and the corresponding perovskite phase when the Cs ratio goes higher than ~30%, while δ-$FAPbI_3$ has lower formation energy than δ-$CsPbI_3$ and the perovskite phase for Cs ratios below ~30% [26,50]. The phase transition energy from the alloyed perovskite phase to the two different non-perovskite phases reaches a minimum at Cs ratio ~30% [26], which is in line with our experimental results in Fig. S7. The $Cs_{2/6}FA_{4/6}PbI_3$ (No.29) perovskite exhibits the lowest content of δ-$CsPbI_3$. The low phase transition energy for FA-rich composition in $Cs_yFA_{1-y}PbI_3$ is also associated with the availability of perovskite phases and gives rise to enhanced stability under our mild preparation conditions. However, Cs-rich ($3/6 \leq y \leq 1$) mixed perovskite phases are enthalpically significantly disfavored [50]. The distortion of the lattice reduces the antibonding overlap of the I p-orbitals with the s-orbitals of Pb of the valence band maximum (VBM) for Cs-rich composition in $Cs_yFA_{1-y}PbI_3$, leading to a less stable structure [33,50]. All of this is also in agreement with their high (FA-based) and low (Cs-based) tolerance factors (Fig. 2). Thus, in $Cs_yFA_{1-y}PbI_3$ ($2/6 \leq y \leq 1$) compositions the perovskite phase could be formed, but it is thermodynamically unstable at room temperature [26,50].[31,50]. All of this is also in agreement with their high (FA-based) and low (Cs-based) tolerance factors (Fig. 2). Thus, in $Cs_yFA_{1-y}PbI_3$ ($2/6 \leqslant y \leqslant 1$) compositions the perovskite phase could be formed, but it is thermodynamically unstable at room temperature [26,50]. Such theoretical prediction is consistent with our experimental results. The crystallographic peaks of I-rich composition No.44-46 with FA^+ as the exclusive A-site cation deviate from other compositions. These films exhibit the characteristic peaks of δ-$FAPbI_3$. In addition, other crystal structures that are not well-defined can be formed (Fig. S2 and S5), originating from low annealing temperature and the formation of an amorphous phase [19,34]. Composition No.44-46 are therefore referred to as an unknow region in our subsequent analysis. With the exception of the seven $Cs_yFA_{1-y}PbI_3$ compositions in the first column, No.44-46 and $Cs_{5/6}FA_{1/6}PbBr_{1/2}I_{5/2}$ (No.9), all other perovskite compositions, crystallize in the perovskite phase. The existence of characteristic peaks at around $q = 1.6$ Å^{-1} and 1.9 Å^{-1} corresponding to the $(210)_T$ and $(211)_T$ reflections, respectively, are used to determine whether a tetragonal phase exists. Similarly, the presence of an additional characteristic peak at around $q = 1.7$ Å^{-1} indexed to the $(211)_O$, $(121)_O$, $(103)_O$ reflections, is utilized to distinguish whether an orthorhombic phase is present. The presence of different perovskite phases is summarized in Fig. 6B and the full set of GIWAXS patterns for all compositions showing the key peaks is given in Fig. S8. The low signal

region for phase identification overlaps with the δ-$CsPbI_3$, making it hard to assess the perovskite phase for compositions No.8, 15, 22, and 29 in $Cs_yFA_{1-y}PbI_3$. Decreased symmetry stemming from the PbX_6 octahedral tilting and distortion has been found in the $Cs_yFA_{1-y}PbI_3$ polycrystalline films upon cesium ratio above 2/6 [33]. The symmetry variation has been well-established in $Cs_yFA_{1-y}PbI_3$ nanocrystals which could stabilize the perovskite phase at room temperature arising from the higher surface/volume ratio, and the crystal symmetry lower from cubic to tetragonal to orthorhombic upon increasing cesium content [43]. This variation of crystal structure conforms to the tendency of tolerance factor which has been corroborated in the literature [26,33,43]. The variation of crystal symmetry in the explored compositional space is consistent with the prediction from the tolerance factors we computed (Fig. 2). Cs-rich compositions with lower tolerance factor (0.8-0.9) have lower crystal symmetry deriving from the size mismatch between A-site cations and PbX_6 octahedra, which are mainly orthorhombic and tetragonal; FA-rich compositions with tolerance factor ~0.9-1.0 have increased crystal symmetry, which are principally tetragonal and cubic. Notably, composition No.36 is identified to have a tetragonal phase and a small amount of δ-$FAPbI_3$ is detected, while composition No.37 forms cubic phase and there is no δ-phase found under our mild preparation condition. This indicates that the incorporation of a small amount of bromine into the crystal lattice can dramatically decrease the phase transition temperature and contribute to the formation of the cubic phase. Hence the correlation between crystal structure and the compositions with varying cesium ratio and bromine ratios is qualitatively established, conducive to help understand the photophysical properties and photovoltaic performance in such materials.

To complement the experimental studies, we have also conducted first-principles density-functional theory calculations to assess the structure of the perovskites and their thermodynamic stability. The optimized lattice constants for all compositions and for the three phases orthorhombic, tetragonal and cubic are shown in Fig. S9. The calculated lattice constants also show the lattice contraction with cesium ratio or bromine ratio increasing, as we observed in XRD and GIWAXS results. Further, using the optimized structures, we compared the phase stability for each composition based on total electronic energy. Results are summarized in Fig. S10. Given the small energy differences between the three phases, we report the thermodynamic stability based on Boltzmann distribution at T = 300℃. As seen from Fig. S10A, for most compositions, more than one phase is thermodynamically stable at room temperature. This suggests that neglected higher

order effects including harmonic and nonharmonic vibrational [51] as well as entropic effects [52], which are computationally non-trivial, can have a noticeable effect in determining the most stable phase. Further, kinetic effects can also be important in determining the most stable phase observed during synthesis.

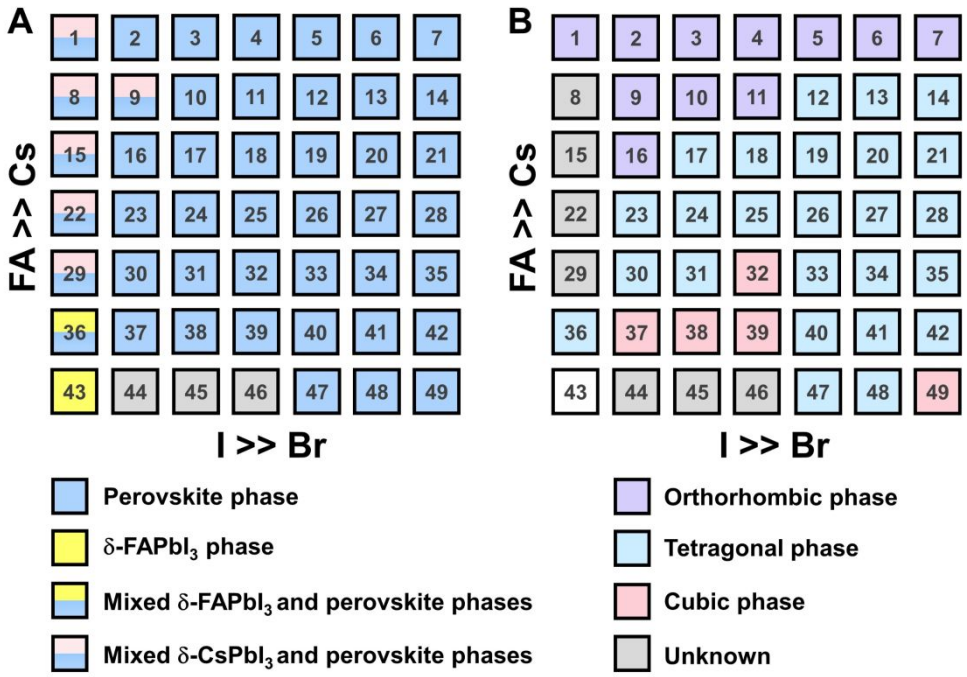

Fig.6 Color map of the presence of perovskite phases (A) and the presence of crystal symmetry for perovskite phases (B) in the $Cs_xFA_{1-x}Pb(Br_yI_{1-y})_3$ compositional space based on the XRD and GIWAXS data. (B) only show the crystal symmetry for perovskite phases in (A) and the empty square for $FAPbI_3$ (No.43) is non-perovskite phase.

Surface morphology

In addition to understanding the structural aspects of these materials, we need to understand film morphology and coverage if we are to fabricate solar cells. Therefore, scanning electron microscopy (SEM) was carried out to image the morphology of the perovskite films in the $Cs_yFA_{1-y}Pb(Br_xI_{1-x})_3$ compositional space. The thickness of the as-deposited perovskite layer is approximately 150-200 nm based on the cross-sectional SEM image (Fig. S11A). The full set of top-view SEM images for the 49 compositions are displayed in Fig. 7. The SEM images at both higher and lower magnifications are available in Fig. S12-S14. The surface morphology of the films shows significant differences among different compositions. Cs-rich compositions (e.g., No. 8-10) exhibit a rough surface with a large degree of pinholes, acting as shunt and moisture pathways, which are detrimental to the performance and stability of the devices [38]. Notably,

variations in the Cs^+/FA^+ ratio in $Cs_yFA_{1-y}PbI_3$ greatly impact the surface morphology. Cs-rich compositions in $Cs_yFA_{1-y}PbI_3$, No.1, No. 8 and No.15, show poorly defined domains and have a large number of pinholes. The δ-$FAPbI_3$ (No.43) presents a rod-like morphology and $Cs_{1/6}FA_{5/6}PbI_3$ (No.36) show defined perovskite domains with average size of 200-300 nm, while $Cs_{3/6}FA_{3/6}PbI_3$ (No.22) and $Cs_{4/6}FA_{2/6}PbI_3$ (No.29) present a combination of rod-shaped crystals embedded among flat domains. The remarkable difference in surface morphology is likely to affect device performances once these films are incorporated in complete solar cell stacks.

There are differences in domain size between the explored compositions. However, there is no clear correlation with increasing bromine or cesium content in the films and domain size. The compositions with high cesium content combined with high bromine content, e.g., $Cs_{5/6}FA_{1/6}PbBr_{3/2}I_{3/2}$ (No.11), $Cs_{5/6}FA_{1/6}PbBr_2I_1$ (No.12), and $Cs_{4/6}FA_{2/6}PbBr_{5/2}I_{1/2}$ (No.20), generally appear to have small domain sizes of ~100 nm. A larger domain size can sometimes be associated with the reduction of the nonradiative recombination and improvement of the charge carrier transport, thus enhancing device performance [53,54]. The films deposited from compositions with low cesium content combined with low bromine content, e.g., $Cs_{2/6}FA_{4/6}PbBr_{1/2}I_{5/2}$ (No. 30), $Cs_{1/6}FA_{5/6}PbI_3$ (No.36), and $Cs_{1/6}FA_{5/6}PbBr_{1/2}I_{5/2}$ (No. 37), have fewer voids and present relatively large domain size, which should lead to higher device efficiencies. The domain size of the film is in line with the reported perovskite films with a similar composition deposited via an analogous approach [27,41].

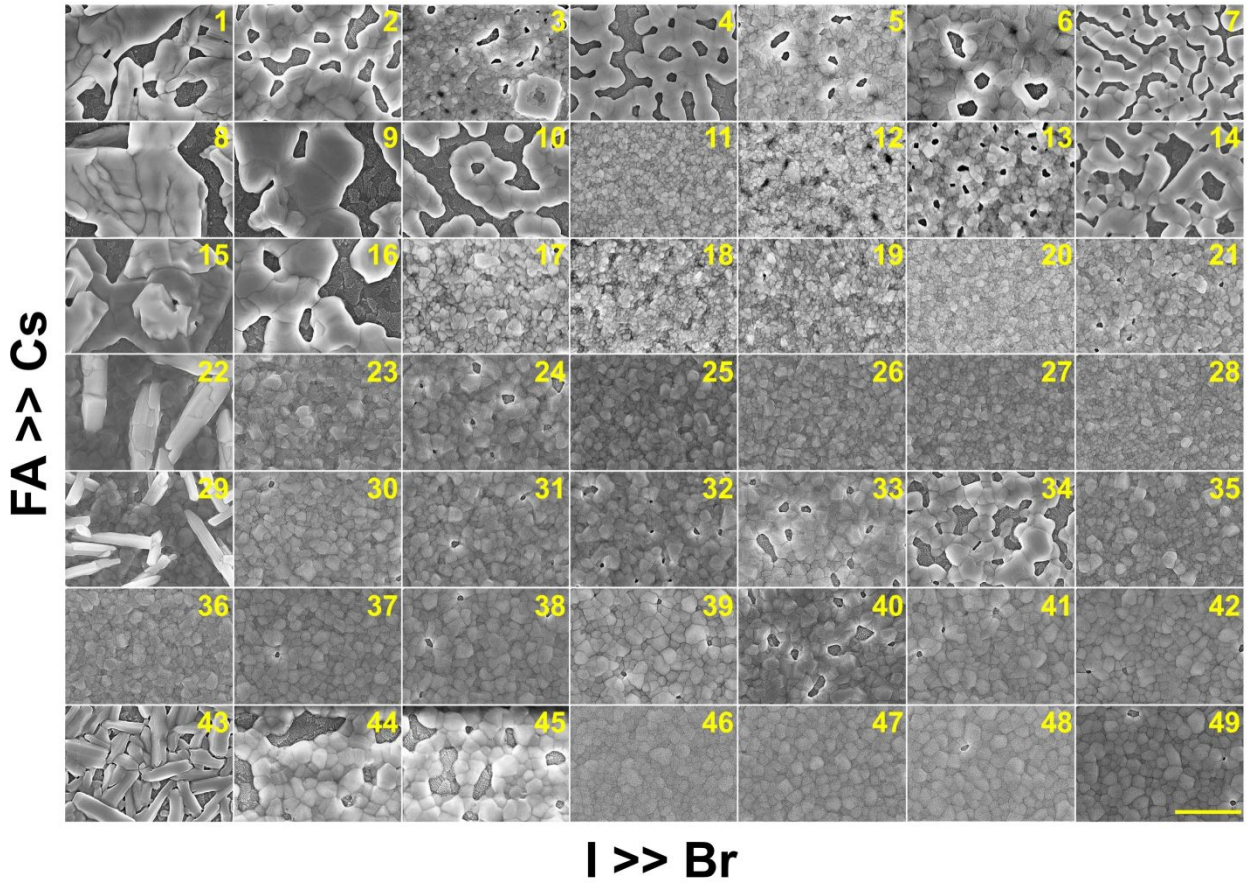

Fig.7. Top-view SEM images of the perovskite films in the $Cs_yFA_{1-y}Pb(Br_xI_{1-x})_3$ compositional space. The panels are arranged in the same order as in the composition matrix of Fig. 1A. The yellow scale bar on the right bottom is 1 μm.

Optical properties

To understand the variations in optical properties in $Cs_yFA_{1-y}Pb(Br_xI_{1-x})_3$ films, ultraviolet-visible absorbance and steady-state photoluminescence (PL) measurements were performed. The absorption and normalized PL as a function of wavelength are presented in Fig. 8 for a subset of the films. The full set of figures for the 49 perovskite films with varying ratios of Cs^+/FA^+ and $Br^-/I^-$are shown in Fig. S15-S18. The absorbance trends observed upon changing the Br^-/I^- ratio are indicated in Fig. 8A. All $Cs_{1/6}FA_{5/6}Pb(Br_xI_{1-x})_3$ films present sharp optical band edges, that will shift to a lower wavelength as the bromine content increases, resulting in bandgap tunability for solar cell application. In addition, the shape of the absorption curve varies with the Br^-/I^-ratio. With higher bromine content, the band edge of absorption becomes sharper and the excitonic absorption appears with the visual appearance of a peak, which is in good agreement with the higher exciton binding energy reported for the Br-rich perovskites [29,55,56]. Changing the Cs^+/FA^+ ratio has a

considerably smaller effect on absorbance than changing the halide ratio, as illustrated in Fig. 8B. When the cesium content is increased, the optical band edges will shift to slightly higher wavelengths. The markedly different impact on the absorbance of $Cs_yFA_{1-y}Pb(Br_xI_{1-x})_3$ thin films when varying Cs^+/FA^+ and Br^-/I^- ratios could be clarified by looking at the contribution of the energy levels of A and X to the electronic band structure of $APbX_3$ [56,57]. As the halide is substituted from I (5p) to Br (4p), the energy of the halide p orbital decreases and Pb-X bond lengths decrease, shifting the VBM toward more negative energy and shifting the CBM toward more positive energy, thus increasing the bandgap [56,57]. Instead, the A-site cations introduce energy levels deep into the bands, and thus do not directly contribute to the VBM and CBM. The A-site cations however have an indirect impact on the bandgap by influencing the Pb-X orbital overlap through two competing effects, i.e., lattice contraction and PbX_6 octahedral tilting [57]. Previous work has shown octahedral tilting is the dominant effect in lead perovskites upon the substitution of the larger FA^+ with the smaller Cs^+ [57]. Octahedral tilting and lowered symmetry reduce the Pb-X orbital overlap, moving the bands to deeper energies and increasing the bandgap for Cs-rich compositions [57].

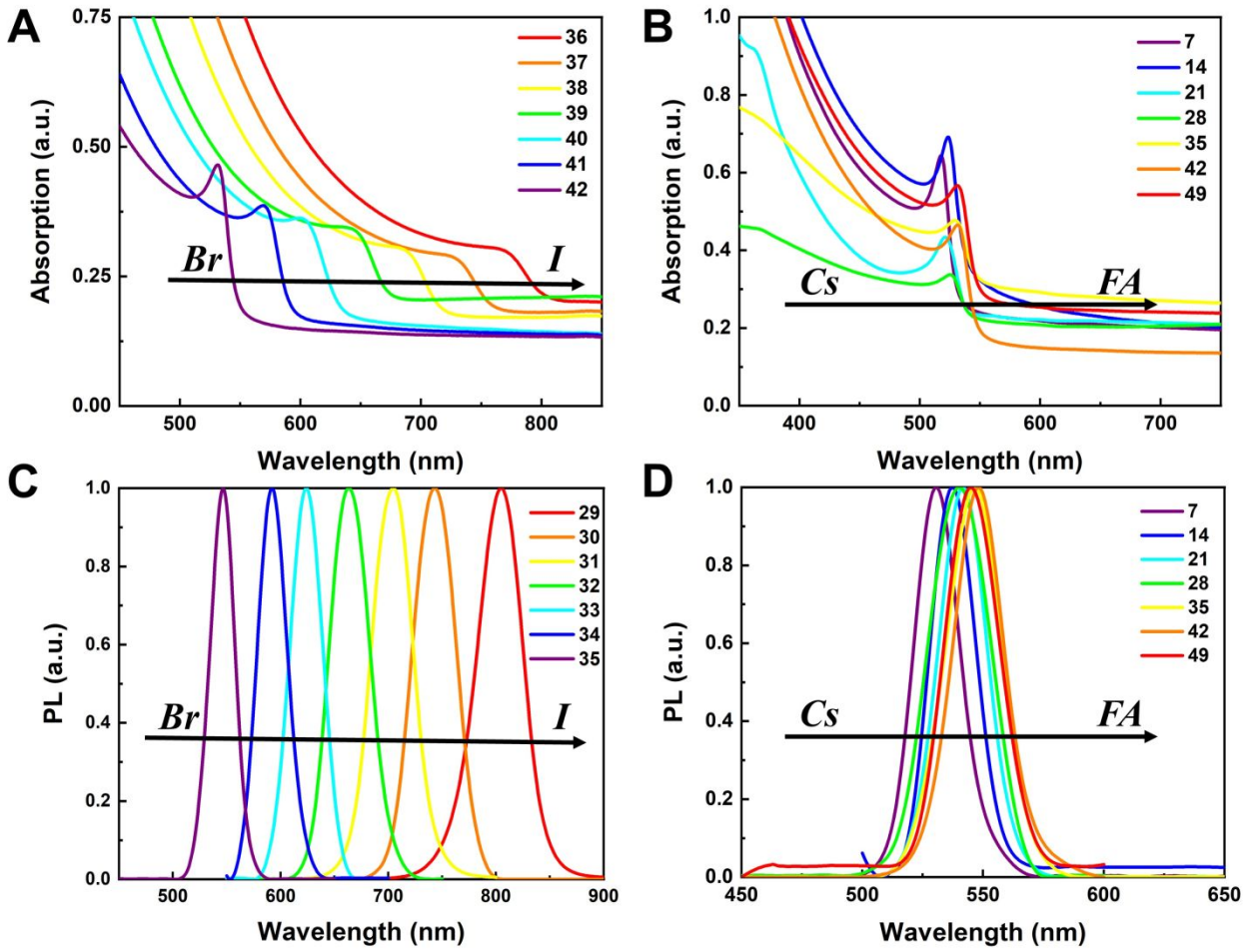

Fig.8. Ultraviolet-visible absorbance spectra of $Cs_{1/6}FA_{5/6}Pb(Br_xI_{1-x})_3$ (A) and $Cs_yFA_{1-y}PbBr_3$ (B) films. Normalized photoluminescence spectra of $Cs_{2/6}FA_{4/6}Pb(Br_xI_{1-x})_3$ (C) and $Cs_yFA_{1-y}PbBr_3$ (D) films.

The trends in PL are in good agreement with the shift of absorption onset, as displayed in Fig. 8C a clear blue shift of PL peak is observed upon increasing the bromine content. The PL peaks of Br-rich samples are narrower than that of I-rich compositions, which can be due to a more defined bandgap without electronic defects. As cesium content increases, the PL peak slightly blue shifts, as can be seen in Fig. 8D and this is consistent with the slight shift in their bandgap. It is worth noting that two PL peaks appear in Br-rich films, e.g., $CsPbBr_2I_1$ (No.5), $Cs_{5/6}FA_{1/6}PbBr_2I_1$ (No.40), and $Cs_{1/6}FA_{5/6}PbBr_{5/2}I_{1/2}$ (No.41) (Fig. S17-S18). From the two peaks, the one at higher energy corresponds to the direct emission from CBM to VBM, but there is also another peak at lower photon energy. This double peak behavior in the Br-rich perovskites is halide phase segregation, which has been reported in previous studies [9,13,29,34]. It was proposed that Br-rich compositions can phase-segregate into majority Br-rich domains with PL peaks at higher energy and minority I-rich domains with PL peak at lower energy upon illumination [9,13,29]. The I-rich

464 domains derive from stochastic composition fluctuations and local lattice strain induced by
465 localized polarons under illumination, which is detrimental to the device performance, especially
466 V_{oc} [15]. The Br-rich compositions with the sub-bandgap photoemission is potentially a problem for
467 the practical application under illumination. From the absorbance spectra, the bandgap energy (E_g)
468 for $Cs_yFA_{1-y}Pb(Br_xI_{1-x})_3$ compositions, as extracted by Tauc plots are summarized in Fig. 9A. The
469 fits used for the calculation are presented in Fig. S19 with the assumption that all compositions are
470 direct bandgap semiconductors. The difference in E_g between a pure iodide perovskite and a pure
471 bromide perovskite with a fixed Cs^+/FA^+ ratio is approximately 0.75 eV, whereas the difference
472 in E_g between a pure Cs perovskite and a pure FA perovskite with a fixed Br^-/I^- ratio is only
473 approximately 0.15 eV.
474 The PL peak positions (E_{PL}) are shown in Fig. 9B. If the composition showed two PL peaks, the
475 one at high energy is the one shown. The compositions with the secondary peak at low photon
476 energy are illustrated in Fig. 9C. A majority of E_{PL} for MA-free $Cs_yFA_{1-y}Pb(Br_xI_{1-x})_3$ matches well
477 to the E_g extracted from the UV-vis measurements, revealing the PL is predominantly from the
478 direct recombination from the CBM to the VBM rather than trap or sub-band states. The energy
479 loss from E_g to E_{PL} for some compositions indicates the emitted photon has less energy than the
480 absorbed photon and the energy loss derives from vibrational relaxation as well as internal
481 conversion, which is called the Stokes shift in PL [58]. Two compositions (i.e., No.6 and No.12)
482 have large energy differences since they exhibit phase segregation during a few minutes of beam
483 exposure during PL measurements (Fig. 9C). There is no second PL peak at low energy in the Br-
484 rich $Cs_yFA_{1-y}PbBr_{3/2}I_{3/2}$ compositions, while the appearance of a second PL peak is documented
485 to appear within a few minutes for $MA_yFA_{1-y}PbBr_{3/2}I_{3/2}$ in literature [29]. This observation possibly
486 aims at the existence of a broader range of photostable compositions for MA-free $Cs_yFA_{1-y}Pb(Br_xI_{1-x})_3$ in comparison to $MA_yFA_{1-y}Pb(Br_xI_{1-x})_3$, though a full understanding of phase
488 segregation is beyond the scope of this initial study. The emitted photon has more energy than the
489 absorbed photon for some compositions and the extra energy comes from the dissipation of thermal
490 phonons in a crystal lattice, this is called up-conversion photoluminescence [58]. PL-peak centered
491 on energies slightly higher than the bandgap energy from absorption also was observed in our
492 previous research [29]. In addition, it has been reported that the perovskite materials show up-
493 conversion properties with phonon-assisted energy gain and potential applications in hot carrier
494 optoelectronic and energy-harvesting devices [59,60].

To quantitatively describe the dependence of E_g on the composition in the $Cs_yFA_{1-y}Pb(Br_xI_{1-x})_3$ space, we fitted an empirical equation to the experimental data. Compositions No.43-46 (I-rich in $FAPb(Br_xI_{1-x})_3$), 8 ($Cs_{5/6}FA_{1/6}PbI_3$), 9 ($Cs_{5/6}FA_{1/6}PbBr_{1/2}I_{5/2}$), 15 ($Cs_{4/6}FA_{2/6}PbI_3$), 16 ($Cs_{4/6}FA_{2/6}PbBr_{1/2}I_{5/2}$) were excluded from the fit. The E_g of compositions No.43-46 follow a different trend than other compositions (Fig. S20A-C), which can be also seen in their crystallographic data. Compositions No.8-9 and No.15-16 show broad absorption without a clear onset (Fig. S15-S16). Under these assumptions, the nonlinear variation of E_g with changing halide ratio could be empirically described via a quadratic equation [12,29]. A quadratic equation also describes the trend in E_g with changes in the ratio of Cs/FA. The E_g across the whole compositional space can then be described with a second-order polynomial:

$$x = \frac{[Br]}{[Br + I]}, y = \frac{[Cs]}{[Cs + FA]}$$

$$E_g(x, y) = 1.50 + 0.56x + 0.08y + 0.19x^2 + 0.11y^2 - 0.10xy \quad (2)$$

The r-square and adjusted r-square of this equitation are 0.976 and 0.973, respectively. The confidence intervals of the determined coefficients are reported in Table S1. Fig. 9D visualizes the comparison between the experimental data of E_g and the empirical equitation of the fit. Notably, the equation can be used to predict the bandgap of the perovskite phase of unexplored compositions. If the equation is used to predict the E_g of $FAPbI_3$, i.e., $x = y = 0$ (composition No.43), which was excluded from our fit being in the δ-phase in our experiment, the estimated E_g will be 1.50 eV, which is in good agreement with the 1.48 eV value reported in literature for the α-phase. The coefficients of the halide ratio variable x are always larger than those of y, again highlighting that an increase in Cs content yields less shift in bandgap than an equivalent increase in Br content. Overall, this equation can be used to estimate the E_g values across the compositional space of $Cs_yFA_{1-y}Pb(Br_xI_{1-x})_3$, and would aid further tailoring E_g for various optoelectronic applications.

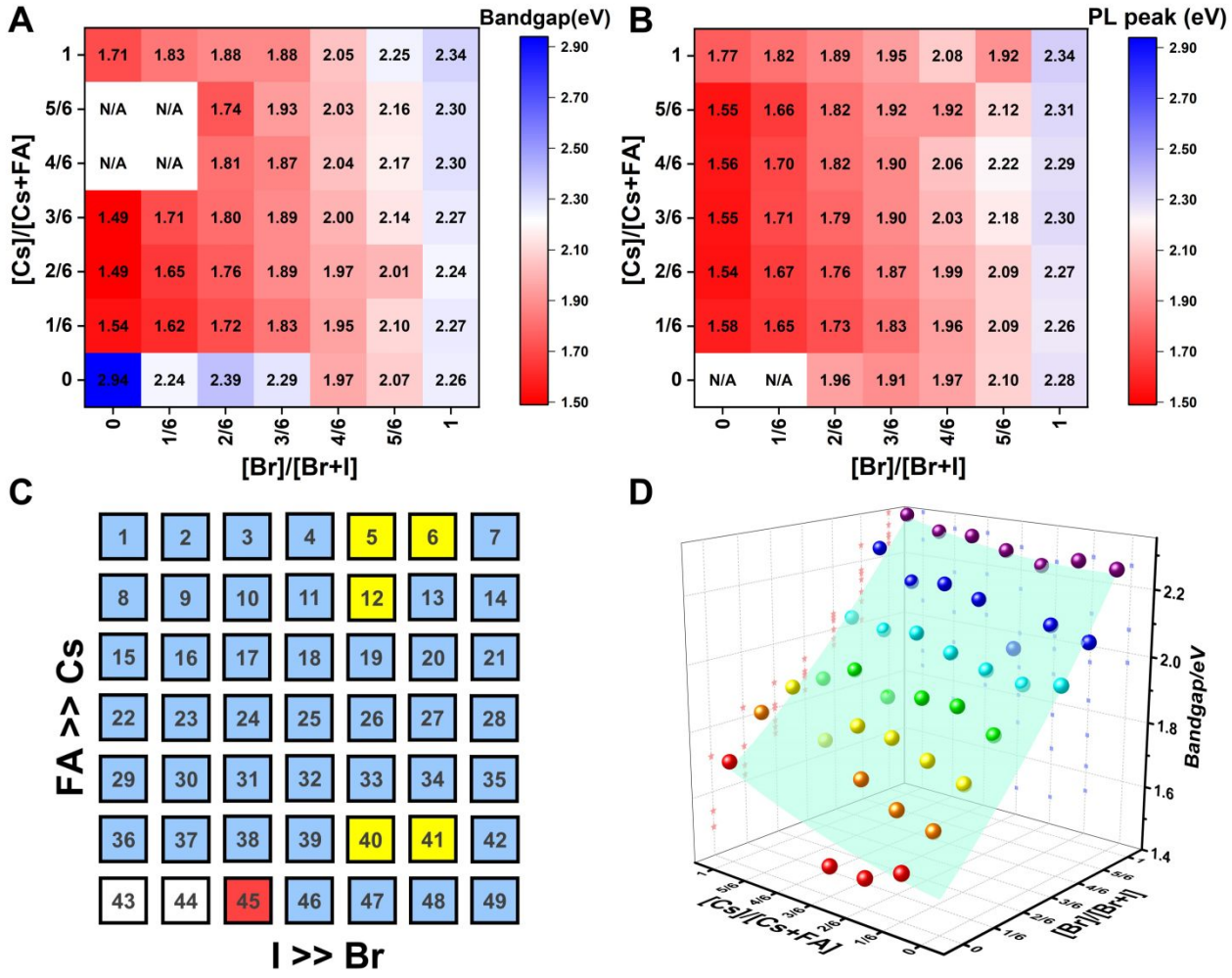

Fig.9. Heat maps of bandgaps extracted from Tauc plots based on absorption (A) and on the PL energy (B) extracted from the wavelength of maximum emission. N/A means not available. Note: if the composition incurred phase segregation and had two peaks, the position of the PL peak at low wavelength was selected. (C) Color map of compositions with phase segregation summarized based on Fig. S16-S17. A blue square means only one peak was observed during the measurement. Yellow square means a secondary PL peak co-exists. Although $CsPbBr_{5/2}I_{1/2}$ (No.6) only has one peak, it is the result of evolving red-shifted PL at low wavelength upon illumination [9]. The red square represents a split PL peak and the white one has no observable PL peaks. (D) Bandgaps as a function of perovskite compositions for the $Cs_yFA_{1-y}Pb(Br_xI_{1-x})_3$ compositional space. The colored dots are the experimental bandgaps calculated from Tauc plots based on absorption. The values predicted from the fitted empirical equation belong to the light green plane in the plot.

Device performance

The I-rich compositions usually yield the highest photovoltaic performance and stability due to the suitable bandgap as photoabsorbers in single junctions solar cells [18,27]. Here, perovskite solar cells for all I-rich compositions $Cs_yFA_{1-y}Pb(Br_xI_{1-x})_3$ ($0 \leq x \leq 3/6$), i.e., first four columns apart

from $CsPbI_3$ and $FAPbI_3$, were fabricated in the n-i-p FTO/c-TiO_2/m-TiO_2/perovskite/Spiro-OMeTAD/Au architecture, where FTO is fluorine-tin-oxide coated glass and Spiro-OMeTAD is 2,2',7,7'-Tetrakis[N,N-di(4-methoxyphenyl)amino]-9,9'-spirobifluorene as the hole transport layer. The perovskite layer in the solar cell was deposited by the same method as the characterized perovskite films. Fig. 10 A-D shows the photovoltaic parameters short-circuit current (J_{sc}), V_{oc}, fill factor (FF), and PCE for reverse scan attained from best devices of each perovskite composition. The corresponding photovoltaic parameters for forward scan and stabilized power output at maximum power point (MPP) are available in Fig. S21. The corresponding box plots, depicting the performance distribution of multiple devices, are given in Fig. S22-S25. The 26 I-rich compositions show a huge spread of device performances, with the reverse PCE varying from 1.30% to 12.25%. Of the 26 I-rich compositions, $Cs_{1/6}FA_{5/6}PbI_3$ (No.36) yielded the best devices, with a reverse PCE of 12.25% and a forward PCE of 12.55%. The best devices have compositions clustered around No.36, involving No.29 ($Cs_{2/6}FA_{4/6}PbI_3$), No 30 ($Cs_{2/6}FA_{4/6}PbBr_{1/2}I_{5/2}$), and No.37 ($Cs_{1/6}FA_{5/6}PbBr_{1/2}I_{5/2}$).

As illustrated in Fig. 10A, when the amount of bromine is increased, there is a decrease in J_{sc} (barring the Cs-rich compositions), directly related to the blue-shift of absorption onset. As cesium ratio increases, a reduction of J_{sc} is observed. This decline is remarkable for compositions with iodide as the exclusive halogen. When the cesium ratio is increased, J_{sc} is significantly decreased from 18.67 mA/cm^2 at y = 1/6 (No.36) to 3.35 mA/cm^2 at y = 5/6 (No.8) for the compositions of $Cs_yFA_{1-y}PbI_3$, while J_{sc} is slightly decreases from 13.30 mA/cm^2 at y = 1/6 (No.38) to 10.38 mA/cm^2 at y = 1 (No.3) for the compositions of $Cs_yFA_{1-y}PbBr_1I_2$. The difference can be attributed to the poor surface morphology of No.8 and No.15 on the one hand, and the presence of a large degree of non-perovskite δ-phase on the other. In light of our recent research work focusing on preferred crystallographic orientation (texture) [61] and its effect on J_{sc}, we analyzed the GIWAXS data, tracking the intensity variations of a specific plane with varying azimuthal angle, as an indication of texture. Our analysis, summarized in Note 1 and Fig. S26-S28, suggests that the impact of texture on the device performance is negligible in the face of other factors, e.g., bandgap, surface morphology, and the existence of lower symmetry phases.

The V_{oc} increases as a result of the widening bandgap with increasing bromine ratio in first three columns (Fig. 10B). Nevertheless, the V_{oc} decreases as the cesium ratio increases, which is in opposite trend to the bandgap. This means that there are additional factors besides the bandgap

that dominate V_{oc}. Besides the poor surface morphology and the presence of δ-phase in Cs-rich compositions the decreased symmetry of Cs-rich compositions is hypothesized to favor non-radiative recombination, inducing a loss in V_{oc}. The Cs-rich compositions have a small tolerance factor, which is representative of a large mismatch in ionic size between the A-site cation and the PbI_6 octahedra. This mismatch leads to lowered symmetry and increased lattice strain, which in turn favors increased defect concentrations and non-radiative recombination, harmful to the V_{oc} [16,62].

The FF of a solar cell is often the most difficult parameter to study and optimize, as it is sensitive to a wide range of loss mechanisms including resistance losses. The FF does not show a clear trend across the compositional space (Fig. 10C). The PCE exhibits a similar functional dependence on the composition as the overall J_{sc} (Fig. 10D), despite the PCE being determined from the products of J_{sc}, V_{oc}, and FF. Increasing the cesium or bromide content decreases the PCE of devices. This suggests that the bandgap variations correlate with the trends in PCE to some extent, which is also expected. Both FA-rich and I-rich compositions exhibit the highest device performance in our study, which can also be attributed to their long carrier lifetime. Rehman et al. extracted the carrier lifetime from photoluminescence decay transients in compositions similar to the ones we report here [31]. The authors found that the region of $0.1 < y < 0.3$ Cs^+ content yielded less non-radiative trap-assisted recombination as well as faster carrier mobility in $Cs_yFA_{(1-y)}Pb(Br_{0.4}I_{0.6})_3$. The carrier lifetime varies from 191 ns for $Cs_{1/6}FA_{5/6}PbI_3$ (No.36) to 22 ns for $Cs_{1/6}FA_{5/6}PbBr_3$ (No.42) perovskite thin films while the carrier diffusion lengths decreased from 4.4 μm for No.36 to 0.8 μm for No.42 in the row of compositions $Cs_{1/6}FA_{5/6}Pb(Br_xI_{1-x})_3$. The longer carrier lifetime in both FA-rich and I-rich compositions is beneficial to the performance of solar cells, which is in line with our device results (Fig. 10).

However, a more insightful way to compare these materials is to normalize by the bandgap. We calculated the ratio of experimental J_{sc}, V_{oc}, and FF, and PCE from the best devices to the corresponding theoretical Shockley-Queisser limit (for each bandgap) of I-rich compositions (Fig. S29) [3]. These ratios can be used to evaluate the loss of each photovoltaic parameter relative to their theoretical value as a function of bandgap. The experimental vs. theoretical ratios in the J_{sc} shown in Fig. S29 are lower than 70% due to reflection from the glass, parasitic absorption by the FTO/TiO_2, and relatively thin layers in these unoptimized devices [63]. However, we plot these ratios for all devices measured to understand trends of J_{sc}. Cs-rich samples, e.g., No.8 and No.9, show

only ~ 12% of the theoretical J_{sc}, mainly deriving from the large amounts of non-perovskite present in the films (Fig. S7). The experimental vs. theoretical ratios in the V_{oc} are also lower than 80% primarily due to trap-assisted non-radiative recombination in the perovskite bulk and interfaces as well as the mismatch of energy level between the perovskite and charge transport layer [64]. Looking at Fig. S29 we can see that moving away from I-rich compositions leads to lower normalized V_{oc}, which suggests that adding Br leads to increased recombination dynamics or a limit by the splitting of the quasi-Fermi levels of the transport layers. These large V_{oc} deficits also occurred in other reported wide-bandgap perovskites [64]. Chemical treatments could remarkably reduce this loss from non-radiative recombination [63,65]. The perovskite fabrication process needs to be optimized together with favorable energy alignment of the contact layers to overcome this loss. Similarly, going from FA- to Cs-rich leads to a decrease in the V_{oc} ratios, which can be attributed to more pinhole formation (Fig. 7). However, looking closer at compositions that have similar morphological features with close bandgap and no non-perovskite phases (Fig. 9A), compositions No. 37, 30, and 23, the V_{oc} decreases with the decrease in symmetry, even though No.23 (1.71eV) has a wider bandgap than No.37 (1.62eV). The V_{oc} goes from cubic and a 70% of theoretical V_{oc} to tetragonal and 61% of theoretical V_{oc} for compositions No. 37 and 23, respectively. It indicates that lower symmetries alone in I-rich perovskites may be one of the factors that lead to lower V_{oc}, which is indicative of increased recombination dynamics. The crystal structure of the perovskite phase seems to have an impact on the device performance and the lower symmetries might lead to increased non-radiative recombination.

Given the promise of the FA-rich I-rich compositions and the thin nature of our films due to poor solubility of CsBr used when processing the films, we set to increase the thickness of the perovskite layer to maximize photon harvesting. Hence, a 1.0 M precursor solution was prepared, and a higher annealing temperature of 150℃ was used to crystallize the deposited films, to suppress the formation of the yellow δ-phase. Fig. 11A shows the champion current-voltage (J-V) characteristic curves for the four compositions (No.29, 30, 36 and 37). The detailed photovoltaic parameters as reported in Table 1. The corresponding box plots and MPP tracking are given in Fig. S30. From the collected data it can be observed that the stabilized power output at MPP of composition No.29 using 1.0 M precursor solution (10.22%) is almost the same as the 0.4 M (10.21%). The negligible change in photovoltaic parameters for this composition, despite the increased thickness and thus the increased GIWAXS signal from the perovskite phases, is to be

ascribed to the presence of a δ-$CsPbI_3$ secondary phase (Fig. S31A-C), which limits performances in spite of the increased thickness and annealing temperature used. The composition PSCs based on No.36 using 1.0 M precursor solution delivers a champion stabilized PCE of 18.62%, benefiting from an improvement in each of the photovoltaic parameters, especially J_{sc} - which raises from 18.67 mA/cm^2 to 24.04 mA/cm^2. As illustrated in Fig.S32, the change in onsets of external quantum efficiency (EQE) spectra for these four compositions match the bandgap extracted from the absorbance onset, E_g (Table. S2). We attribute the enhancement to the absence of δ-phase (Fig. S31A-B) for this composition. The stabilized PCE of composition No.30 and No.37 also raise to 15.13% and 17.13%, respectively. The increase in annealing temperature does not change the preferred crystallographic orientation and crystal symmetry of No.30, No.36, and No.37, still keeping the cubic, tetragonal and cubic structure, respectively (Fig. S31). The long-term operational stability data obtained for PSC with composition No.36 and No.37 held at MPP under 1 sun irradiation in nitrogen atmosphere and at room temperature are shown in Fig. 11B. After 330 h, the solar cell with composition No.36 retained 94% of its initial efficiency. The major contribution to the efficiency drop observed is attributed to a 5% decrease in V_{oc} and FF compared to the initial values (Fig. S33). The solar cell with composition No.37 maintained 98% of the initial efficiency exhibiting increased photostability, which is of promise to enable solar cells with long-term stability. No.36 (1.54 eV) and No.37 (1.62 eV) not only have suitable bandgaps to absorb the light illumination, but also exhibits less mismatch in crystal structure that gives rise to the suppression of non-perovskite phase, thus leading to their high performance and durable among the compositions explored. It is the structure and optoelectronic properties that determine the optimized composition for making high performance devices.

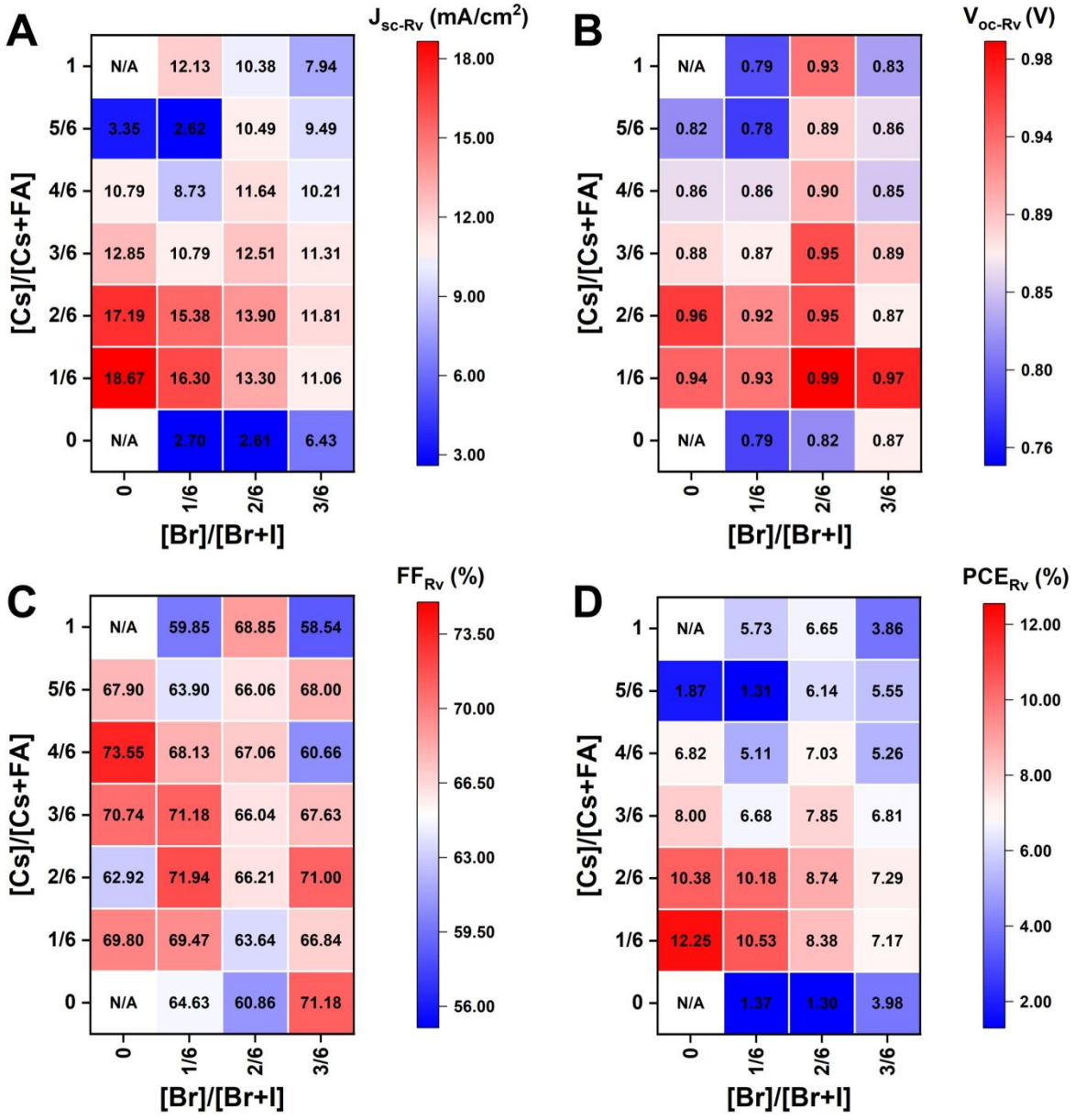

Fig.10. The photovoltaic parameters of J_{sc} (A), V_{oc} (B), FF (C), and PCE (D) for reverse scan attained from best devices of I-rich compositions using 0.4 M perovskite precursor solutions.

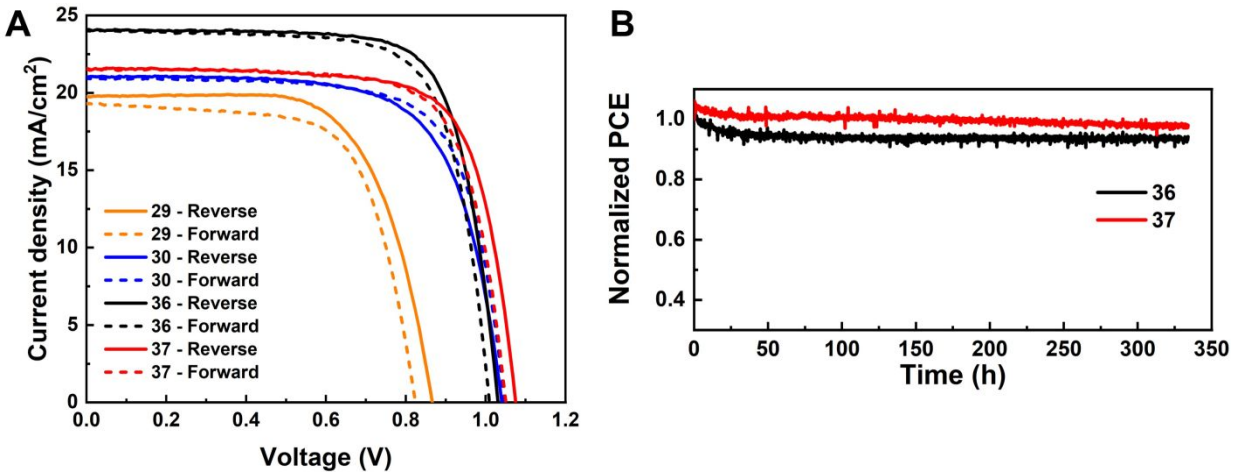

Fig. 11. (A) Reverse J-V curves of the champion PSCs of composition 29, 30, 36, and 37 using 1.0 M perovskite precursor solutions with 5% excess Pb^{2+}. (B) Continuous MPP tracking results under 1 sun irradiance at N_2 atmosphere of devices of composition 36 and 37.

Table 1. Photovoltaic parameters of champion devices based on composition 29, 30, 36 and 37 measured under AM 1.5G illumination

Composition	29	30	36	37
$J_{sc\text{-}Rv}$ (mA/cm^2)	19.76	21.03	24.04	21.57
$V_{oc\text{-}Rv}$ (V)	0.86	1.04	1.03	1.08
FF_{Rv}(%)	66.95	69.19	74.66	73.08
PCE_{Rv}(%)	11.38	15.13	18.49	17.03
$J_{sc\text{-}Fw}$ (mA/cm^2)	19.30	20.94	24.02	21.55
$V_{oc\text{-}Fw}$ (V)	0.83	1.05	1.01	1.05
FF_{Fw}(%)	66.79	71.62	73.03	73.52
PCE_{Fw}(%)	10.70	15.75	17.72	16.64
Stabilized MPP (%)	10.22	15.13	18.62	17.13

Our work illustrates the importance of the precise composition on structural integrity of the perovskite structure, including segretation into non-perovskite phases and Br- and I-rich perovskites. These are all important aspects for device operation. Compositional changes allow us to to tailor the crystallographic properties and improve the structural stability of perovskite materials. The phase separation phenomenon could be suppressed by incorporating Br^- and limited Cs^+, as well as increasing the crystallization temperature. For instance, No. 37 ($Cs_{1/6}FA_{5/6}PbBr_{1/2}I_{5/2}$) with the incorporated Br^- shows no δ-phase compared with No.36

($Cs_{1/6}FA_{5/6}PbI_3$) annealed at 65 ℃ in Fig. 5A. Thus, the content of δ-$FAPbI_3$ in No.36 is significantly decreased when the Cs^+ substitutes FA^+ and the films are annealed at 65 ℃ (Fig. S7). In addition, the δ-$FAPbI_3$ is removed in composition No. 36 when the samples are annealed at 150 ℃. Moving away from pure iodine compounds ($x \geqslant 1/6$), no δ-phases detected, with the exception of the $Cs_{5/6}FA_{1/6}PbBr_{1/2}I_{5/2}$ (No.9) and unknown No.44-46. Interestingly, the δ-$CsPbI_3$ still exists for Cs-rich compositions (e.g. No.29) with I^- as the exclusive X-site halide even though annealed at 150 ℃ (Fig. S31C). There is no appearance of the δ-phase in No.30 ($Cs_{2/6}FA_{4/6}PbBr_{1/2}I_{5/2}$) with the incorporation Br^- compared with No.29 ($Cs_{1/6}FA_{5/6}PbI_3$) even when annealed at 65 ℃ (Fig. 6A). Thus, the thermodynamic stability of the perovskite material itself at room temperature is critical to its properties. Concerning the optical and crystallographic properties for solar cell applications, the optimal Br ratio needs to include a analysis of the trade-off between the opposing effects, i.e., the widening of the bandgap and the enhanced structural stability, which believe is in the compositions No.36 and No.37.

Conclusions

Through the systematic exploration of the MA-free $Cs_yFA_{1-y}Pb(Br_xI_{1-x})_3$ compositional space, we have revealed structure-property relationships by combining crystallographic and optoelectronic characterization. We qualitatively discussed the correlation between the Goldschmidt tolerance factor and experimentally identified crystal structures. We showed that Cs-rich compositions exhibit significant phase separation into perovskite phase and non-perovskite δ-phase alongside poor surface morphology, which resulted in low efficiencies once the layers were incorporated in full solar cell stacks. However, there are indications that lower symmetries alone in Cs-rich perovskites lead to lower open-circuit voltages, which is indicative of increased recombination dynamics. In I-rich perovskite compositions, it was found that the bandgap, phase purity and surface morphology of the perovskite phase dominate the performance. Of the explored perovskite compositions, $Cs_{1/6}FA_{5/6}PbI_3$ and $Cs_{1/6}FA_{5/6}PbBr_{1/2}I_{5/2}$ yield the highest efficiencies and operational stability, showing the greatest promise as a material for optoelectronic devices. A concomitant tuning of the charge selective layers for proper energy level alignment to these optimized perovskites may be required in future applications. This work highlights the significance of compositional design to improve the optoelectronic performances of perovskite films, and shows how the analysis of the structure-property relationship for a class of materials can be used to provide deeper insight of their optoelectronic properties.

Acknowledgment:

This work was performed in part at the Georgia Tech Institute for Electronics and Nanotechnology, a member of the National Nanotechnology Coordinated Infrastructure (NNCI), which is supported by the National Science Foundation (Grant ECCS-1542174). J.P.C.B., Y.A., C.A.R.P., J.H., A.F.C.M., J.N.V., and C.E. thank Georgia Institute of Technology for the financial support. Y.A. thanks the financial support from China Scholarship Council (CSC) fellowship (No. 201906250003). W.A.S. acknowledge support from U. S. National Science Foundation (Award No. CSSI-2003808). Also, we are grateful for computing time provided in part by the Pittsburgh Center for Research Computing (CRC) resources at the University of Pittsburgh. X.L. and S.W. acknowledge financial support from the National Science Foundation of China (No. 21676188). This research used CMS beamline of the National Synchrotron Light Source II, a U.S. Department of Energy (DOE) Office of Science User Facility operated for the DOE Office of Science by Brookhaven National Laboratory under Contract No. DE-SC0012704.

Reference

1 A. Kojima, K. Teshima, Y. Shirai and T. Miyasaka, *J. Am. Chem. Soc.*, 2009, **131**, 6050–6051.

2 H. Min, D. Y. Lee, J. Kim, G. Kim, K. S. Lee, J. Kim, M. J. Paik, Y. K. Kim, K. S. Kim, M. G. Kim, T. J. Shin and S. Il Seok, *Nat. 2021 5987881*, 2021, **598**, 444–450.

3 S. Rühle, *Sol. Energy*, 2016, **130**, 139–147.

4 M. Saliba, T. Matsui, J.-Y. Y. Seo, K. Domanski, J.-P. P. Correa-Baena, M. K. Nazeeruddin, S. M. Zakeeruddin, W. Tress, A. Abate, A. Hagfeldt and M. Grätzel, *Energy Environ. Sci.*, 2016, **9**, 1989–1997.

5 J. P. Correa-Baena, M. Saliba, T. Buonassisi, M. Grätzel, A. Abate, W. Tress and A. Hagfeldt, *Science*, 2017, **358**, 739–744.

6 K. Xiao, R. Lin, Q. Han, Y. Hou, Z. Qin, H. T. Nguyen, J. Wen, M. Wei, V. Yeddu, M. I. Saidaminov, Y. Gao, X. Luo, Y. Wang, H. Gao, C. Zhang, J. Xu, J. Zhu, E. H. Sargent and H. Tan, *Nat. Energy*, 2020, **5**, 870–880.

7 J. Xu, C. C. Boyd, Z. J. Yu, A. F. Palmstrom, D. J. Witter, B. W. Larson, R. M. France, J. Werner, S. P. Harvey, E. J. Wolf, W. Weigand, S. Manzoor, M. F. A. M. Van Hest, J. J. Berry, J. M. Luther, Z. C. Holman and M. D. McGehee, *Science*, 2020, **367**, 1097–1104.

8 D. P. McMeekin, G. Sadoughi, W. Rehman, G. E. Eperon, M. Saliba, M. T. Hörantner, A. Haghighirad, N. Sakai, L. Korte, B. Rech, M. B. Johnston, L. M. Herz and H. J. Snaith, *Science*, 2016, **351**, 151–155.

9 R. E. Beal, D. J. Slotcavage, T. Leijtens, A. R. Bowring, R. A. Belisle, W. H. Nguyen, G. F. Burkhard, E. T. Hoke and M. D. McGehee, *J. Phys. Chem. Lett.*, 2016, **7**, 746–751.

10 J. J. Yoo, G. Seo, M. R. Chua, T. G. Park, Y. Lu, F. Rotermund, Y.-K. K. Kim, C. S. Moon, N. J. Jeon, J.-P. P. Correa-Baena, V. Bulović, S. S. Shin, M. G. Bawendi and J. Seo, 2021, **590**, 587–593.

11 B. Conings, J. Drijkoningen, N. Gauquelin, A. Babayigit, J. D'Haen, L. D'Olieslaeger, A. Ethirajan, J. Verbeeck, J. Manca, E. Mosconi, F. De Angelis and H. G. Boyen, *Adv. Energy Mater.*, 2015, **5**, 1–8.

12 J. H. Noh, S. H. Im, J. H. Heo, T. N. Mandal and S. Il Seok, *Nano Lett.*, 2013, **13**, 1764–1769.

13 E. T. Hoke, D. J. Slotcavage, E. R. Dohner, A. R. Bowring, H. I. Karunadasa and M. D. McGehee, *Chem. Sci.*, 2015, **6**, 613–617.

14 S. J. Yoon, M. Kuno and P. V. Kamat, *ACS Energy Lett.*, 2017, **2**, 1507–1514.

15 C. G. Bischak, C. L. Hetherington, H. Wu, S. Aloni, D. F. Ogletree, D. T. Limmer and N. S. Ginsberg, *Nano Lett.*, 2017, **17**, 1028–1033.

16 S. Mahesh, J. M. Ball, R. D. J. Oliver, D. P. McMeekin, P. K. Nayak, M. B. Johnston and H. J. Snaith, *Energy Environ. Sci.*, 2020, **13**, 258–267.

17 S. M. Yoon, H. Min, J. B. Kim, G. Kim, K. S. Lee and S. Il Seok, *Joule*, 2021, **5**, 183–196.

18 J. J. Yoo, G. Seo, M. R. Chua, T. G. Park, Y. Lu, F. Rotermund, Y. K. Kim, C. S. Moon, N. J. Jeon, J. P. Correa-Baena, V. Bulović, S. S. Shin, M. G. Bawendi and J. Seo, *Nature*, 2021, **590**, 587–593.

19 G. E. Eperon, S. D. Stranks, C. Menelaou, M. B. Johnston, L. M. Herz and H. J. Snaith, *Energy Environ. Sci.*, 2014, **7**, 982–988.

20 H. Min, M. Kim, S. U. Lee, H. Kim, G. Kim, K. Choi, J. H. Lee and S. Il Seok, *Science*, 2019, **366**, 749–753.

21 M. Saliba, T. Matsui, K. Domanski, J. Y. Seo, A. Ummadisingu, S. M. Zakeeruddin, J. P. Correa-Baena, W. R. Tress, A. Abate, A. Hagfeldt and M. Grätzel, *Science*, 2016, **354**, 206–209.

22 G. Kieslich, S. Sun and A. K. Cheetham, *Chem. Sci.*, 2014, **5**, 4712–4715.

23 G. E. Eperon, G. M. Paternò, R. J. Sutton, A. Zampetti, A. A. Haghighirad, F. Cacialli and H. J. Snaith, *J. Mater. Chem. A*, 2015, **3**, 19688–19695.

24 N. J. Jeon, J. H. Noh, W. S. Yang, Y. C. Kim, S. Ryu, J. Seo and S. Il Seok, *Nature*, 2015, **517**, 476–480.

25 C. C. Stoumpos, C. D. Malliakas and M. G. Kanatzidis, *Inorg. Chem.*, 2013, **52**, 9019–9038.

26 Z. Li, M. Yang, J. S. Park, S. H. Wei, J. J. Berry and K. Zhu, *Chem. Mater.*, 2016, **28**, 284–292.

27 K. A. Bush, K. Frohna, R. Prasanna, R. E. Beal, T. Leijtens, S. A. Swifter and M. D. McGehee, *ACS Energy Lett.*, 2018, **3**, 428–435.

28 A. Binek, F. C. Hanusch, P. Docampo and T. Bein, *J. Phys. Chem. Lett.*, 2015, **6**, 1249–1253.

29 T. Jesper Jacobsson, J. P. Correa-Baena, M. Pazoki, M. Saliba, K. Schenk, M. Grätzel and A. Hagfeldt, *Energy Environ. Sci.*, 2016, **9**, 1706–1724.

30 G. Niu, H. Yu, J. Li, D. Wang and L. Wang, *Nano Energy*, 2016, **27**, 87–94.

31 W. Rehman, D. P. McMeekin, J. B. Patel, R. L. Milot, M. B. Johnston, H. J. Snaith and L. M. Herz, *Energy Environ. Sci.*, 2017, **10**, 361–369.

32 J. W. Lee, D. H. Kim, H. S. Kim, S. W. Seo, S. M. Cho and N. G. Park, *Adv. Energy Mater.*, , DOI:10.1002/aenm.201501310.

33 C. Yi, J. Luo, S. Meloni, A. Boziki, N. Ashari-Astani, C. Grätzel, S. M. Zakeeruddin, U. Röthlisberger and M. Grätzel, *Energy Environ. Sci.*, 2016, **9**, 656–662.

34 W. Rehman, R. L. Milot, G. E. Eperon, C. Wehrenfennig, J. L. Boland, H. J. Snaith, M. B. Johnston and L. M. Herz, *Adv. Mater.*, 2015, **27**, 7938–7944.

35 J. P. Correa-Baena, Y. Luo, T. M. Brenner, J. Snaider, S. Sun, X. Li, M. A. Jensen, N. T. P. Hartono, L. Nienhaus, S. Wieghold, J. R. Poindexter, S. Wang, Y. S. Meng, T. Wang, B. Lai, M. V. Holt, Z. Cai, M. G. Bawendi, L. Huang, T. Buonassisi and D. P. Fenning, *Science*, 2019, **363**, 627–631.

36 G. Kim, H. Min, K. S. Lee, D. Y. Lee, S. M. Yoon and S. Il Seok, *Science*, 2020, **370**, 108–112.

37 R. D. Shannon, *Acta Crystallogr. Sect. A*, 1976, **32**, 751–767.

38 Y. An, J. Hidalgo, C. A. R. Perini, A.-F. Castro-Méndez, J. N. Vagott, K. Bairley, S. Wang, X. Li and J.-P. Correa-Baena, *ACS Energy Lett.*, 2021, 1942–1969.

39 J. A. Vigil, A. Hazarika, J. M. Luther and M. F. Toney, *ACS Energy Lett.*, 2020, **5**, 2475–2482.

40 Q. Zhao, A. Hazarika, L. T. Schelhas, J. Liu, E. A. Gaulding, G. Li, M. Zhang, M. F. Toney, P. C. Sercel and J. M. Luther, *ACS Energy Lett.*, 2020, **5**, 238–247.

41 R. E. Beal, N. Z. Hagström, J. Barrier, A. Gold-Parker, R. Prasanna, K. A. Bush, D. Passarello, L. T. Schelhas, K. Brüning, C. J. Tassone, H. G. Steinrück, M. D. McGehee, M. F. Toney and A. F. Nogueira, *Matter*, 2020, **2**, 207–219.

42 B. Charles, M. T. Weller, S. Rieger, L. E. Hatcher, P. F. Henry, J. Feldmann, D. Wolverson and C. C. Wilson, *Chem. Mater.*, 2020, **32**, 2282–2291.

43 J. A. Vigil, A. Hazarika, J. M. Luther and M. F. Toney, *ACS Energy Lett.*, 2020, **5**, 2475–2482.

44 B. Zhao, S. F. Jin, S. Huang, N. Liu, J. Y. Ma, D. J. Xue, Q. Han, J. Ding, Q. Q. Ge, Y. Feng and J. S. Hu, *J. Am. Chem. Soc.*, 2018, **140**, 11716–11725.

45 A. Marronnier, G. Roma, S. Boyer-Richard, L. Pedesseau, J.-M. M. Jancu, Y. Bonnassieux, C. Katan, C. C. Stoumpos, M. G. Kanatzidis and J. Even, *ACS Nano*, 2018, **12**, 3477–3486.

46 J. A. Steele, H. Jin, I. Dovgaliuk, R. F. Berger, T. Braeckevelt, H. Yuan, C. Martin, E. Solano, K. Lejaeghere, S. M. J. Rogge, C. Notebaert, W. Vandezande, K. P. F. Janssen, B. Goderis, E. Debroye, Y. K. Wang, Y. Dong, D. Ma, M. Saidaminov, H. Tan, Z. Lu, V. Dyadkin, D. Chernyshov, V. Van Speybroeck, E. H. Sargent, J. Hofkens and M. B. J. Roeffaers, *Science*, 2019, **365**, 679–684.

47 M. Rodová, J. Brožek, K. Knížek and K. Nitsch, *J. Therm. Anal. Calorim.*, 2003, **71**, 667–673.

48 M. Zhang, Z. Zheng, Q. Fu, Z. Chen, J. He, S. Zhang, L. Yan, Y. Hu and W. Luo, *CrystEngComm*, 2017, **19**, 6797–6803.

49 E. C. Schueller, G. Laurita, D. H. Fabini, C. C. Stoumpos, M. G. Kanatzidis and R. Seshadri, *Inorg. Chem.*, 2018, **57**, 695–701.

50 A. Boziki, D. J. Kubicki, A. Mishra, S. Meloni, L. Emsley, M. Grätzel and U. Rothlisberger, *Chem. Mater.*, 2020, **32**, 2605–2614.

51 T. Tadano and S. Tsuneyuki, *Phys. Rev. B - Condens. Matter Mater. Phys.*, 2015, **92**, 054301.

52 W. A. Saidi and J. J. Choi, *J. Chem. Phys.*, 2016, **145**, 144702.

53 H. Li, G. Wu, W. Li, Y. Zhang, Z. Liu, D. Wang and S. Liu, *Adv. Sci.*, 2019, **6**, 1901241.

54 A. F. Castro-Méndez, J. Hidalgo and J. P. Correa-Baena, *Adv. Energy Mater.*, 2019, 9, 1901489.

55 S. Zhang, H. Liu, X. Li and S. Wang, *Nano Energy*, 2020, **77**, 105302.

56 V. K. Ravi, G. B. Markad and A. Nag, *ACS Energy Lett.*, 2016, **1**, 665–671.

57 R. Prasanna, A. Gold-Parker, T. Leijtens, B. Conings, A. Babayigit, H. G. Boyen, M. F. Toney and M. D. McGehee, *J. Am. Chem. Soc.*, 2017, **139**, 11117–11124.

58 X. Zhu, Q. Su, W. Feng and F. Li, *Chem. Soc. Rev.*, 2017, **46**, 1025–1039.

59 J. Yang, X. Wen, H. Xia, R. Sheng, Q. Ma, J. Kim, P. Tapping, T. Harada, T. W. Kee, F. Huang, Y.-B. Cheng, M. Green, A. Ho-Baillie, S. Huang, S. Shrestha, R. Patterson and G. Conibeer, *Nat. Commun. 2017 81*, 2017, **8**, 1–9.

60 A. Granados del Águila, T. T. H. Do, J. Xing, W. J. Jee, J. B. Khurgin and Q. Xiong, *Nano Res. 2020 137*, 2020, **13**, 1962–1969.

61 J. Hidalgo, C. A. R. R. Perini, A.-F. F. Castro-Mendez, D. Jones, H. Köbler, B. Lai, R. Li, S. Sun, A. Abate and J.-P. P. Correa-Baena, *ACS Energy Lett.*, 2020, **5**, 3526–3534.

62 M. I. Saidaminov, J. Kim, A. Jain, R. Quintero-Bermudez, H. Tan, G. Long, F. Tan, A. Johnston, Y. Zhao, O. Voznyy and E. H. Sargent, *Nat. Energy*, 2018, **3**, 648–654.

63 R. He, S. Ren, C. Chen, Z. Yi, Y. Luo, H. Lai, W. Wang, G. Zeng, X. Hao, Y. Wang, J. Zhang, C. Wang, L. Wu, F. Fu and D. Zhao, *Energy Environ. Sci.*, , DOI:10.1039/D1EE01562A.

64 M. Jošt, L. Kegelmann, L. Korte and S. Albrecht, *Adv. Energy Mater.*, 2020, **10**, 1904102.

65 S. Masi, A. F. Gualdrón Reyes and I. Mora-Seró, *ACS Energy Lett.*, 2020, **5**, 1974–1985.